Generated using the official AMS LaTeX template v6.1

Impacts of stochastic coalescence variability on warm rain initiation using Lagrangian microphysics in box and large-eddy simulations

Hugh Morrison[a] , Kamal Kant Chandrakar[a] , Shin-Ichiro Shima[b] , Piotr Dziekan[c] , Wojciech W. Grabowski[a]

[a] *National Science Foundation National Center for Atmospheric Research, Boulder, CO USA*

[b] *Graduate School of Information Science, University of Hyogo, Kobe, Japan*

[c] *Institute of Geophysics, Faculty of Physics, University of Warsaw, Warsaw, Poland*

Corresponding author: Hugh Morrison, morrison@ucar.edu

ABSTRACT: Various coalescence methods for Lagrangian microphysics schemes are tested in box and large-eddy simulation (LES) models, including the stochastic all-or-nothing super-droplet method (SDM) and a version of SDM (dSDM) that applies a fractional approach similar to the average impact method. In LES, variabilities driven by microphysics and by flow realizations are separated using the "piggybacking" technique. Rain initiation averaged over many realizations of the box model is delayed and rain variability increases as the number of super-drops per collision volume (N_{SD}) is decreased using SDM. In contrast, rain initiation time using SDM in LES is insensitive to N_{SD} for $32 \leq N_{SD} \leq 512$. This is explained through the interaction between LES grid boxes, each acting as a separate collision volume. Variability across the ensemble of LES collision volumes using SDM results in rain quickly initiating in some of the LES grid cells at low N_{SD} and leading to a similar overall timing of rain initiation from the cloud compared to simulations with high N_{SD}. There is a ~20% decrease in the total rain mass and mean rain flux as N_{SD} is increased from 32 to 256, with little additional change as N_{SD} is increased from 256 to 512. The fractional coalescence approach in dSDM leads to reduced microphysical variability and a 15-18 min delay in rain initiation compared to SDM. An additional LES ensemble with microphysical variability feeding back to the dynamics shows that flow variability dominates the impact of microphysical variability on rain properties. Thus, flow variability must be constrained to isolate impacts of microphysical variability.

SIGNIFICANCE STATEMENT: An emerging tool in cloud microphysics modeling represents drops by computational particles called "super-droplets" that evolve in the modeled flow. Recent studies have documented that different super-droplet models produce widely varying predictions of rain. Understanding these differences is an important step in the wider adoption of these models by the community. Here we examine different methods for representing droplet collision-coalescence in a super-droplet model and sensitivity to the number of super-droplets employed. The timing of rain initiation is insensitive to super-droplet number in 3D cloud simulations, but rain is substantially delayed using a coalescence method that limits random variability in droplet collisions. We also show that flow variability must be constrained to isolate impacts of microphysical variability on rain properties.

1. Introduction

A problem that has spanned decades of research concerns the timing of rain onset in warm clouds via drop collision-coalescence (hereafter "coalescence"). Some studies have considered this problem from the standpoint of coalescence statistics (e.g., Kostinski and Shaw 2005; Wilkinson 2016). Statistical fluctuations in the number of coalescence events drops experience can drive rapid growth of some drops, which is accelerated by the nonlinear relationship between drop radius and collection kernel (Telford 1955). That is, a tiny fraction of drops will happen to experience a much higher number of coalescence events than the expected value, and these drops can rapidly grow to raindrop sizes. Such drops undergoing a much higher number of coalescence events than expected have been referred to as "lucky drops". It has been argued in several papers that lucky drops are a key factor controlling rain initiation in warm clouds (e.g., Telford 1955; Twomey 1966; Kostinski and Shaw 2005; Wilkinson 2016).

Most cloud models use bulk or bin microphysics schemes to represent microphysical processes, including drop coalescence. Such schemes treat cloud and precipitation particles with Eulerian variables corresponding to extensive microphysical properties, and they do not explicitly account for coalescence fluctuations. In contrast to traditional bulk and bin schemes, a markedly different Lagrangian approach for microphysics has emerged within the past decade that represents hydrometeors in cloud models as discrete point particles (e.g., Shima et al. 2009; Sölch and Kärcher 2010; Riechelmann et al. 2012; Unterstrasser and Sölch 2014; Arabas et al. 2015; Naumann and

Seifert 2015; Hoffmann et al. 2015; Dziekan and Pawlowska 2017; Jaruga and Pawlowska 2018; Brdar and Seifert 2018; Grabowski et al. 2018; Hoffmann et al. 2019; Shima et al. 2020; Chandrakar et al. 2021). Each of these computational particles, referred to as "super-droplets" (SDs) or "super-particles", represents some multitude of real particles (the number of real particles each SD represents is called *multiplicity*). The SDs follow Lagrangian trajectories in the modeled flow, and each SD tracks various properties such as drop mass and multiplicity. Lagrangian particle-based schemes have several conceptual and practical advances compared with traditional Eulerian schemes (see Grabowski et al. 2019). Most relevant to the current paper, they can explicitly represent statistical fluctuations in coalescence (e.g., Shima et al. 2009) that may be critical to initiating rain as discussed above. Bin microphysics schemes solve the deterministic Smoluchowski equation, which is a mean field equation. This equation does not consider coalescence fluctuations explicitly but does represent all probabilities and collision paths that produce lucky drops via a continuous distribution function; in effect, the Smoluchowski equation corresponds to an infinite collision volume in which all collision probabilities are realized.

Different methods have been proposed to treat drop coalescence in Lagrangian schemes. These include the super-droplet method (SDM) of Shima et al. (2009), also referred to as "all-or-nothing", in which coalescence events are treated probabilistically. If a coalescence event is realized, all drops comprising the SD with smaller multiplicity of the interacting SD pair grow by collecting drops from the other SD. The re-mapping algorithm (Andrejczuk et al. 2010) collects all SDs within a collision volume (usually assumed to be one model grid cell), maps them to a binned distribution, solves the coalescence using a traditional bin-based approach, and then resamples the updated distribution to obtain a corresponding set of SDs. The average impact method (AIM; Riechelmann et al. 2012; Maronga et al. 2015) calculates coalescence growth of collector drops by assuming some fraction of drops within each SD pair coalesce every time step as long as the collection kernel of the interacting drops is greater than zero. The mass of coalesced drops is distributed evenly among all drops comprising the collector SD (in AIM, the collector SD is the one with larger drops in the interacting SD pair). This approach, which will be referred to as *fractional* coalescence, is purely deterministic; the number of drops coalesced for every SD pair at each time step is equal to the expected value. Because of this, and because all drops comprising the collector SD grow at the same rate, AIM is inherently limited in its ability to represent lucky

drops compared to SDM. Note that the Smoluchowski equation is also deterministic, but has a continuous representation of the DSD in contrast to the discrete representation in AIM via its finite number of Lagrangian SDs. As a consequence, whereas AIM is limited in its ability to represent lucky drops, the Smoluchowski equation represents all possible pathways to their formation by evolving a DSD distribution function.

Unterstrasser et al. (2017) examined these Lagrangian particle-based methods in a set of zero-dimensional box model tests using the well-known kernels of Golovin (1963), Long (1974), and Hall (1980). These tests specified an initial DSD and examined its evolution by coalescence with all other processes neglected. They found large differences using these methods, with SDM giving the best performance overall relative to analytic or benchmark numerical solutions. Unterstrasser et al. (2020) tested different configurations of SDM in box and one-dimensional (1D) models (allowing drop transport via sedimentation), again with coalescence being the only process considered. Results were sensitive to the number of SDs in a grid cell, N_{SD}, and to a lesser extent the time step and vertical grid spacing. A key result of Unterstrasser et al. (2020) was that convergence of solutions was much faster as N_{SD} was increased (i.e., it occurred at lower N_{SD}) in the 1D model than the box model because of SD transport via sedimentation; they found that using $N_{SD} = 24$ yielded reasonable results with the 1D model. This was explained by SDs in the 1D model not being confined to the same grid cell, which greatly increased the number of potential collision pairs and thus, in effect, increased the degrees of freedom. Schwenkel et al. (2018) reached a similar conclusion regarding the impact of SD transport on convergence behavior. Although there is some agreement concerning the numerical behavior and convergence of coalescence methods in Lagrangian schemes, a recent intercomparison study using box and 1D models showed surprisingly large differences in solutions from two models that both used SDM with the same collection kernel (Hill et al. 2023). It was hypothesized that these differences may have arisen from using different SD initialization methods or other details of the numerical implementation, which was found to be important in box model tests of Unterstrasser et al. (2017).

Other recent studies have specifically examined aspects of stochastic coalescence using SDM. Dziekan and Pawlowska (2017, hereafter DP2017) analyzed statistics related to rain initiation time and lucky drops from an ensemble of simulations using a box model corresponding to a well-mixed volume. They showed a substantially slower mean rain initiation time in small volumes,

corresponding to small total drop number N_{tot}. Results approached solutions of the Smoluchowski equation for large collision volumes and N_{tot}, with relatively fast rain initiation. Variability in rain initiation time, quantified by relative standard deviation (ensemble standard deviation divided by mean), also decreased with an increase in N_{SD} by a factor roughly proportional to $N_{SD}^{-1/2}$ when keeping the ratio N_{SD}/N_{tot} constant. This is consistent with excessive variance in the number of coalescence events using SDM (Shima et al. 2009, see also section 2 herein). DP2017 also found that SDM with multiplicity of 1 for all SDs (meaning each SD represents a single real drop) could reproduce statistics of lucky drops consistent with the analytic estimate of Kostinski and Shaw (2005). Li et al. (2022), using box and 1D tests to examine stochastic coalescence, also found that SDM could accurately reproduce coalescence fluctuations and lucky drop statistics at low SD multiplicity.

Although several studies have simulated precipitating clouds using 2D or 3D dynamical models with Lagrangian microphysics (e.g., Andrejczuk et al. 2010; Riechelmann et al. 2012; Arabas and Shima 2013; Hoffmann et al. 2015; Grabowski et al. 2018; Hoffmann et al. 2017; Noh et al. 2018; Dziekan et al. 2019; Shima et al. 2020; Dziekan et al. 2021; Chandrakar et al. 2021, 2022), few have specifically focused on the impact of stochastic coalescence in such models. A challenge is separating the impact of flow variability driven by the dynamics from microphysical variability driven by stochastic coalescence. Zmijewski et al. (2023) used the "piggybacking" technique (e.g., Grabowski 2014; Grabowski and Jarecka 2015; Grabowski and Morrison 2016) to separate microphysical and dynamical variability. Piggybacking involves running a model with two (or more) different sets of cloud and thermodynamic variables – one set coupled to the dynamics in a two-way feedback, and the other(s) simply responding to the flow but not feeding back to it. This allows testing different microphysical configurations with the same flow field. Zmijewski et al. (2023) focused mainly on convergence with respect to time step and N_{SD} in box tests and 2D piggybacking simulations. Even with a constrained flow field, convergence was not achieved in the 2D simulations with N_{SD} up to 10^5 in cases with lighter precipitation. Spatial variability of rain decreased with increasing N_{SD}, which Zmijewski et al. (2023) suggested led to more precipitation with increasing N_{SD} and lack of convergence in bulk rain properties.

The main goal of our study is to extend the previous work summarized above on Lagrangian microphysics to examine different coalescence methods and sensitivity to N_{SD} in 3D LES of

a cumulus congestus cloud. Box model simulations are also performed to verify results from previous box studies and provide context for our LES results. Similar to Zmijewski et al. (2023), we employ piggybacking to isolate variability driven by the microphysics from variability driven by different flow realizations. In addition to testing the standard SDM and AIM approaches for coalescence, we test a new method – a deterministic version of SDM (dSDM) – to further elucidate the impact of stochastic coalescence fluctuations in SDM on rain initiation. dSDM is deterministic and applies fractional coalescence similar to AIM. Thus, it is also inherently limited in its ability to represent lucky drops, although it differs from AIM in allowing smaller drops in the SD pair to grow as collector drops as in SDM (see section 2 for details). Comparing dSDM and SDM allows for a direct assessment of the impacts of Monte Carlo all-or-nothing versus fractional coalescence methods, with all else being equal.

There are several specific science questions addressed in the current paper:

- What is the impact of stochastic fluctuations in coalescence on rain initiation using the Monte Carlo all-or-nothing approach in SDM compared to the fractional approach in AIM and dSDM?
- How is the simulated evolution of cloud and rain using the various coalescence methods sensitive to changes in N_{SD}?
- How do the impact of stochastic coalescence fluctuations, sensitivity to N_{SD}, and numerical convergence differ between the box model and LES?
- How does variability introduced by coalescence fluctuations in SDM compare to variability associated with different flow realizations induced by perturbed initial conditions and microphysics-dynamics feedback?

The main novel aspects of this work are the use of both box and 3D LES frameworks to examine different coalescence methods and sensitivity to N_{SD}. While piggybacking was employed previously by Zmijewski et al. (2023) to separate microphysical and flow variability, here we use piggybacking in a 3D LES rather than 2D cloud model. Furthermore, we focus on testing various coalescence methods to understand impacts of coalescence variability as well as sensitivity to N_{SD}; Zmijewski et al. (2023) were primarily concerned with sensitivity to N_{SD}, time step, and SD initialization.

The rest of the paper is organized as follows. Section 2 describes the coalescence methods and provides theoretical context. Section 3 gives an overview of the box model experimental design and results. A description of the LES and results are presented in section 4. Section 5 gives a summary, discussion and conclusions.

2. Description of the coalescence methods and theoretical considerations

We test several different methods for calculating collision-coalescence in Lagrangian particle-based microphysics schemes. Two of the methods tested are SDM (Shima et al. 2009) and AIM (Riechelmann et al. 2012; Maronga et al. 2015), which were briefly discussed in the introduction. We also test a deterministic version of SDM (dSDM). A conceptual diagram with an example of how these three methods work is given in Fig. 1, with a mathematical description given below. Here, we restrict the description to the case when coalescence probability of the interacting SD pair $P^*_{ij} \leq 1$ for simplicity, with modifications for $P^*_{ij} > 1$ described later.

a. SDM

Consider a pair of ith and jth SDs within a collision volume that may potentially collide. For SDM, coalescence of the SDs is realized when $\phi < P^*_{ij}$, where $\phi \in [0,1]$ is a uniform random number and P^*_{ij} is the coalescence probability of the ith and jth SDs:

$$P^*_{ij} = \max\left(M_i, M_j\right) P_{ij}. \tag{1}$$

Here M_i and M_j are the multiplicities of the ith and jth SDs and P_{ij} is the coalescence probability of individual drops comprising the SDs over time step Δt:

$$P_{ij} = K_{ij}\Delta t / V \tag{2}$$

where V is the collision volume and

$$K_{ij} = E\pi\left(r_i + r_j\right)^2 \left|v_i - v_j\right| \tag{3}$$

is the gravitational collision kernel, E is the collection efficiency (coalescence efficiency is assumed to be unity), r_i and r_j are the drop radii of the ith and jth SDs, and v_i and v_j are the drop fall speeds. Note that implementing turbulence-induced collision enhancement in Lagrangian particle-based schemes may accelerate rain formation, especially when other DSD broadening mechanisms are limited (Hoffmann et al. 2017), but this aspect is not investigated here and we focus solely on gravitational collection. Because we apply gravitational collection and all drops represented by an individual SD are assumed to have uniform size and fallspeed, coalescence of drops within a SD is neglected.

The standard configuration of SDM also applies a stochastic linear sampling of drop coalescence pairs to improve efficiency. In this sampling, a list of $N_{SD}/2$ random, non-overlapping SD pairs is generated. By "non-overlapping", we mean that no SD belongs to more than one pair. This procedure costs $O(N_{SD})$ in computation as opposed to $O(N_{SD}^2)$ when dealing with all possible $N_{SD}\,(N_{SD}-1)$ collision pairs with "full sampling". The linear sampling requires a scaling of P_{ij}^* to account for fewer pairs being sampled relative to the total number of all pairs (see Shima et al. 2009). The scaled-up probability is $P'_{ij} = P_{ij}^* \frac{N_{SD}(N_{SD}-1)}{2} / \left(\frac{N_{SD}}{2}\right)$. In the box model tests in section 3, we examine both SDM with linear sampling and with full sampling of SD pairs. The description below is for full sampling with P_{ij}^*, which allows a more straightforward comparison with AIM (which also applies full sampling of SD pairs). For SDM with linear sampling, P_{ij}^* is replaced with P'_{ij}.

If coalescence between the ith and jth SDs is realized, the SDs change their state after they coalesce (see middle column of SD pairs in Fig. 1 for an illustration). In this case, taking $M_j > M_i$, then

$$\Delta M_j = -M_i \tag{4}$$

$$\Delta m_i = m_j \tag{5}$$

where ΔM and Δm are the change in multiplicity and drop mass as a result of the coalescence event, and subscripts indicate the ith or jth SD.

When coalescence is realized and $M_i = M_j$, then no drops are left in either the ith or jth SD because all drops in the SD pair contribute to coalescence. In this case, the resulting coalesced droplets are divided evenly into the ith and jth SDs (see eqs. 16-19 in Shima et al. 2009).

When $M_i = M_j = 1$, SDM with full sampling of SD pairs is equivalent to a primitive model (see section 2.1.4 in Shima et al. 2009) that represents coalescence of all individual drops in a collision volume based on the premise that this can be represented probabilistically and drops are well-mixed in the volume. In this case, $P^*_{ij} = P_{ij}$ and the statistical behavior of the model corresponds to that expected for a population of real world drops coalescing with probability P_{ij}.

b. Deterministic SDM

We formulate a deterministic version of SDM, hereafter dSDM. This is identical to SDM except that instead of drawing a uniform random number to determine if a coalescence event is realized, whereby $\min\left(M_i, M_j\right)$ coalescence events occur for individual drops comprising the SD pair, a number of drops $\leq \min\left(M_i, M_j\right)$ comprising part of the collectee SD are coalesced at every time step so long as $K_{ij} > 0$ (right column of SD pairs in Fig. 1). The fraction of drops coalesced from the collectee SD (with larger multiplicity) is distributed evenly among the drops comprising the collector SD (with smaller multiplicity), i.e., fractional coalescence. For every coalescence pair, the state of the SDs are updated every time step similar to eqs. 4-5, except that the all-or-nothing stochastic Monte Carlo scheme in SDM is replaced by the coalescence probability P^*_{ij}. Taking $M_j > M_i$, this gives

$$\Delta M_j = -M_i P^*_{ij} = -K_{ij} M_i M_j \Delta t / V \tag{6}$$

$$\Delta m_i = m_j P^*_{ij} = m_j K_{ij} M_j \Delta t / V. \tag{7}$$

c. AIM

For AIM, which is deterministic and uses fractional coalescence like dSDM, coalescence of a number of drops $\leq \min\left(M_i, M_j\right)$ comprising part of the collectee SD occurs for every SD pair as long as $K_{ij} > 0$. The coalesced mass of collectee drops is distributed among all drops in the collector SD (see left column of SD pairs in Fig. 1 for an illustration). However, AIM differs from dSDM in how the collectee and collector SDs are determined. We again consider coalescence of the ith and jth SDs within a collision volume, and here choose i and j such that $m_i > m_j$. At each time step, the SDs change their state following eqs. 25 and 26 from Unterstrasser et al. (2017), which can be rewritten as (neglecting collisions of same-sized drops, i.e., first term on the r.h.s. of

eq. 25 therein):

$$\Delta M_j = -M_i P^*_{ij} = -K_{ij} M_i M_j \Delta t / V \tag{8}$$

$$\Delta m_i = m_j P^*_{ij} = m_j K_{ij} M_j \Delta t / V. \tag{9}$$

The coalescence of drops and transfer of drop number and mass between the ith and jth SDs is identical between AIM and dSDM when $m_i > m_j$ and $M_j > M_i$ (eqs. 8-9 are identical to eqs. 6-7). In contrast, when $m_i > m_j$ and $M_j < M_i$, the coalescence of drops between the ith and jth SDs differs between AIM and dSDM (eqs. 8-9 differ from eqs. **??**-**??**); also compare the left and right columns in Fig. 1. This difference occurs because AIM assumes that all *i* drops with *larger size* in the SD pair grow at the average rate, while dSDM assumes that all drops with *smaller multiplicity* grow at the average rate. In essence, AIM sorts by droplet size (or mass) while dSDM sorts by multiplicity. AIM never decreases multiplicity of the *i* drops (larger drops) in the SD pair. This arises from the assumption in AIM that all collector drops in the SD pair (i.e., the larger drops) grow at the same rate regardless of the multiplicities. In contrast, dSDM decreases M_i or M_j, whichever multiplicity is larger, regardless of drop size. Implications of this difference are discussed later.

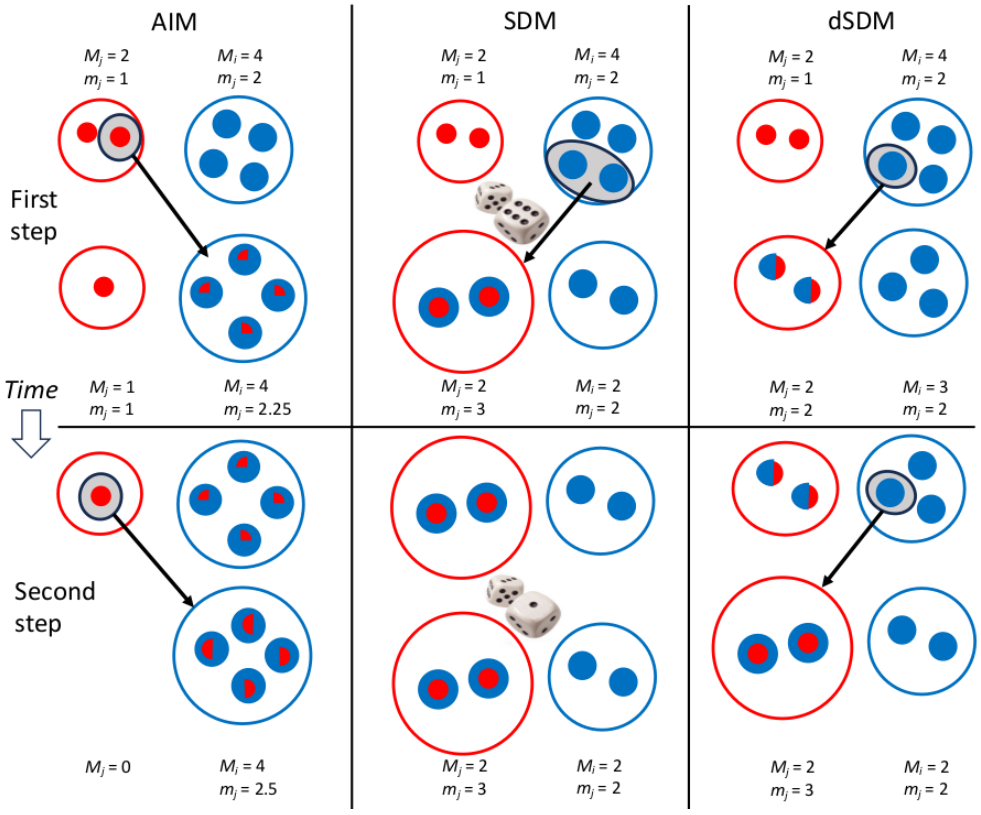

FIG. 1. Conceptual diagram of the three main methods for modeling coalescence in this study (inspired by Fig. 2 in Unterstrasser et al. 2017): 1) average impact method (AIM, left column), 2) super-droplet method (SDM, middle column), and 3) deterministic super-droplet method (dSDM, right column). The initial multiplicity M_i and M_j and initial mass m_i and m_j of the SD pair are given near the top, and SD evolution is illustrated for two time steps. The expected number of coalesced drops is equal to unity for each time step. In the first step, fractional coalescence in AIM leads to growth of drops comprising the SD with larger drops (blue circle), while fractional coalescence in dSDM leads to growth of drops for the SD with smaller multiplicity (red circle). In this example, coalescence is realized during the first step with the Monte Carlo (symbolized by dice) all-or-nothing approach in SDM, leading to rapid growth of drops comprising the SD with smaller multiplicity (red circle). In the second time step, fractional growth continues for AIM and dSDM while coalescence is not realized in SDM. All three methods are consistent with the expected number of coalescence events averaged over both time steps, such that 4 drops remain with a total mass $m_i + m_j = 10$. However, the final mass distribution of drops is different in AIM than SDM and dSDM, while in this example it is the same in SDM and dSDM. For a system of many SDs, in SDM there will be a distribution in the number of coalescence events around the expected value, and as a result it will produce different results than dSDM (since dSDM as well as AIM are consistent with the expected value for all SD pairs at every time step).

d. Case of multiple coalescence

The descriptions of SDM, dSDM, and AIM above strictly apply when the coalescence probability over Δt is ≤ 1. Shima et al. (2009) extended the Monte Carlo approach in SDM to account for multiple coalescence events of a single drop within the SD pair that occur when $P^*_{ij} > 1$. This situation might be expected if Δt is too large, particular for SD pairs when K_{ij} is large. One approach is to simply reduce Δt such that $P^*_{ij} \leq 1$ for physical consistency. Note there may still be sensitivity of solutions to Δt in this case, mainly because it is assumed that drops only collide with a single other drop over Δt. Thus, in principle SDM should be increasingly accurate as $\Delta t \rightarrow 0$. Alternatively, Shima et al. (2009) introduced an integer parameter γ that represents the number of times each collector drop in the SD pair coalesces. This is defined as $\gamma = 1 + \left[P^*_{ij}\right]$ when the $[0, 1]$ uniform random number $\phi < P^*_{ij} - \left[P^*_{ij}\right]$, and $\gamma = \left[P^*_{ij}\right]$ when $\phi \geq P^*_{ij} - \left[P^*_{ij}\right]$. Here Gauss's symbol $[x]$ is the greatest integer that is less than or equal to real number x. In effect, when $P^*_{ij} > 1$, the fraction $\left[P^*_{ij}\right] / P^*_{ij}$ of possible coalescence events is treated deterministically (i.e., coalescence occurs regardless of ϕ), while the remaining fraction $1 - \left[P^*_{ij}\right] / P^*_{ij}$ is treated probabilistically and depends on ϕ. The total number of coalescence events over Δt for the SD pair is restricted to be less than or equal to $\max\left(M_i, M_j\right) / \min\left(M_i, M_j\right)$ to prevent more drops being coalesced than exist.

For dSDM, multiple coalescence is treated simply by allowing $P^*_{ij} > 1$ in eqs. 6-**??**. As in SDM, the total number of coalescence events over Δt for the SD pair is also restricted to be less than or equal to $\max\left(M_i, M_j\right) / \min\left(M_i, M_j\right)$. For AIM, multiple coalescence is treated similarly by allowing $K_{ij}\Delta t / V > 1$ in eqs. 8-9, but restricting the number of coalescence events to be less than or equal to M_j / M_i (where $m_i > m_j$).

e. Comparison of SDM, dSDM, and AIM in a theoretical context

As detailed by Shima et al. (2009), the expected value for the number of coalescence events in SDM is identical to that of the primitive model (and thus real world). Considering interaction of ith and jth SDs, in the real world this corresponds to $M_i M_j$ pairs of drops that may possibly coalesce. The number of drop pairs that coalesce is therefore described by a binomial distribution with $M_i M_j$ independent trials with success probability $P_{ij} = K_{ij}\Delta t / V$. It follows that the expected number of coalescence events in the real world is $M_i M_j K_{ij}\Delta t / V$. For coalescence of drops comprising a SD pair using dSDM, the number of actual coalescence events is $\min\left(M_i, M_j\right) P^*_{ij}$, which follows from

Shima et al. (2009) for SDM. This gives a number of coalescence events equal to $M_i M_j K_{ij} \Delta t / V$ regardless of whether $M_i > M_j$ or $M_j > M_i$ (taking $m_i > m_j$). Thus, dSDM is also consistent with the expected number of coalescence events in the real world. Similarly, the number of coalescence events for AIM is $M_i M_j K_{ij} \Delta t / V$ following eq. 8, also consistent with the real world. Linear sampling of SD pairs does not affect the expected number of coalescence events compared to full sampling.

In the real world, each coalescence event is a binary event involving i and j groupings of drops, which implies that a number $M_i M_j K_{ij} \Delta t / V$ of i drops coalesce with the same number of j drops over Δt (neglecting drops that coalesce with multiple other drops over Δt). However, because the transfer of mass is spread across all i or j collector drops in dSDM or all i collector drops in AIM (again choosing $m_i > m_j$), this leads to inconsistency for both methods even though they give the correct expected number of coalescence events compared to the real world. That is, both methods give the correct reduction of drop number from coalescence, but in general they spread the coalesced mass over a larger number of collector drops than should occur. Error from this inconsistency is larger in AIM than dSDM, which is explained as follows. First, take the case when $M_j > M_i$, keeping in mind that $m_i > m_j$. The mass of j drops coalesced is added uniformly to all i drops in both AIM and dSDM, implying M_i number of coalescence events has occurred. This leads to an inconsistency when $-\Delta M_j = M_i M_j K_{ij} \Delta t / V < M_i$, or analogously $M_j K_{ij} \Delta t / V < 1$, because the actual number of coalescence events is less than M_i. The ratio of implied number of coalescence events to the actual number is $M_i / \left(M_i M_j K_{ij} \Delta t / V \right) = 1 / \left(M_j K_{ij} \Delta t / V \right)$ for both dSDM and AIM. Thus, error is identical for dSDM and AIM when $M_j > M_i$, and when $M_j K_{ij} \Delta t / V$ is small, error is large.

Now consider the case when $M_i > M_j$. For dSDM, the mass of i drops collected is added uniformly to all j drops, implying M_j number of coalescence events. This leads to an inconsistency when $-\Delta M_i = M_i M_j K_{ij} \Delta t / V < M_j$, or analogously $M_i K_{ij} \Delta t / V < 1$. The ratio of implied number of coalescence events to the actual number is $M_j / \left(M_i M_j K_{ij} \Delta t / V \right) = 1 / \left(M_i K_{ij} \Delta t / V \right)$. In contrast, AIM adds mass uniformly to all i drops, implying M_i number of coalescence events. Thus, AIM gives a ratio of implied number of coalescence events to actual number of $M_i / \left(M_i M_j K_{ij} \Delta t / V \right) = 1 / \left(M_j K_{ij} \Delta t / V \right)$. Since $M_j < M_i$ in this instance, error is larger for AIM than SDM by a factor of M_i / M_j when $M_i > M_j$.

SDM avoids this inconsistency entirely by assuming all i drops or all j drops within a SD pair coalesce if a probabilistic coalescence event is realized. In that case, the (average) implied number of coalescence events is exactly equal to the expected number. In summary, it follows from the above discussion that dSDM is expected to give more accurate results than AIM overall. However, the most important coalescence events leading to rain initiation are likely when $m_i > m_j$ and $M_j > M_i$ (i.e., multiplicity decreasing with drop radius), in which case AIM and dSDM are identical.

As mentioned in the introduction, a well known feature of SDM is its excessive variance in the number of coalescence events compared to the primitive model or real world. As explained in Shima et al. (2009), variance in number of coalescence events in the real world is $M_i M_j P_{ij}\left(1 - P_{ij}\right) \approx M_i M_j P_{ij}$ in the Poisson distribution limit with small P_{ij}. In SDM, the variance is $\left(\min\left(M_i, M_j\right)\right)^2 P^*_{ij} - \left(M_i M_j P_{ij}\right)^2 \approx \min\left(M_i, M_j\right) M_i M_j P_{ij}$. Thus, variance in the number of coalescence events in SDM is approximately $\min\left(M_i, M_j\right)$ times larger than that of the real world. Stochastic linear sampling of SD pairs introduces additional coalescence variability, although we show in section 3 that this does not contribute much to overall microphysical variability compared to the Monte Carlo coalescence scheme in SDM.

AIM and dSDM with full sampling of SD pairs have no variance from the coalescence process; they are fully deterministic. However, both AIM and dSDM can be used with stochastic linear sampling of SD pairs, which introduces some stochastic variability and hence non-zero variance. In addition to SDM with linear sampling (which we will refer to simply as "SDM"), tests described in sections 3 and 4 include dSDM with stochastic linear sampling, which we call LSdSDM (linearly sampled dSDM). In this way, comparing LSdSDM with SDM can isolate impacts of the Monte Carlo all-or-nothing versus fractional coalescence schemes, while applying the same stochastic linear sampling of SD pairs in both. Linear sampling greatly reduces the computational cost compared to full sampling, which is an important consideration for the LES. To isolate the impact of the stochastic linear sampling further, an additional set of box model tests is performed using AIM but including stochastic linear sampling of SD pairs, which will be referred to as LSAIM (linearly sampled AIM). In both LSdSDM and LSAIM, the probability P^*_{ij} is replaced with P'_{ij} to account for fewer SD pairs being sampled. Finally, we test SDM with full sampling (fSDM) using the box model. Following the standard SDM approach (Shima et al. 2009), multiplicities are

rounded to the nearest integer for all box model and LES tests herein. A summary of the different configurations tested herein is given in Table 1.

TABLE 1. Summary of the various microphysics configurations tested herein. Coalescence method refers to the fractional versus stochastic all-or-nothing (AON) approaches. "SD growth based on multiplicity versus mass" refers to the method for determining which SD in the coalescence pair serves as the collector, based on whether the SD has either lower multiplicity or larger mass (see section 2 text for details).

Name	Coalescence method	Sampling of SD coalescence pairs	SD growth based on multiplicity versus mass
SDM	Stochastic AON	Linear	Multiplicity
fSDM	Stochastic AON	Full	Multiplicity
dSDM	Fractional	Full	Multiplicity
LSdSDM	Fractional	Linear	Multiplicity
AIM	Fractional	Full	Mass
LSAIM	Fractional	Linear	Mass

3. Box model simulations

a. Box model description and setup

The box model setup is similar to previous zero-dimensional box model studies evaluating coalescence using Lagrangian particle-based schemes (e.g., Unterstrasser et al. 2017; Hoffmann et al. 2017; Li et al. 2022; Zmijewski et al. 2023). Only coalescence is considered and all other physical processes are neglected. Six model configurations discussed in section 2 are tested: SDM, fSDM, dSDM, LSdSDM, LSAIM, and AIM (see Table 1). An additional set of simulations using the primitive model, with each SD representing a single physical drop and applying full sampling of coalescence pairs, gives results close to fSDM when the total number of drops in the primitive model, N_{tot}, is $\approx N_{SD}$ in fSDM (not shown). SDM also produces similar results to the primitive model when $N_{tot} \approx N_{SD}$. The Hall (1980) collection kernel is used for all simulations presented herein (both box and LES).

As initial conditions for the box model, we specify a gamma DSD. The gamma DSD N' is characterized by

$$N' = N_0 r^{\mu} e^{-\lambda r} \tag{10}$$

where r is drop radius and N_0, λ, and μ are the intercept, slope, and shape parameters of the distribution, respectively. We present results using inverse exponential initial DSDs (gamma DSD with $\mu = 0$). Tests with other shape parameters of the gamma DSD give qualitatively similar results. We can integrate Eq. 10 to calculate various distribution moments from which we can derive bulk physical quantities of the DSD, such as total drop number and mean drop radius r_m:

$$N_{tot} = \frac{N_0 \Gamma(\mu+1)}{\lambda^{\mu+1}} \tag{11}$$

$$r_m = \frac{\Gamma(\mu+2)}{\Gamma(\mu+1)\lambda} = \frac{\mu+1}{\lambda} \tag{12}$$

where N_{tot} is the total droplet number in the collision volume and Γ is the Euler gamma function. In this approach we specify N_{tot}, r_m, and μ. By combining eqs. 11 and 12 and rearranging terms, we can obtain N_0 and λ from N_{tot}, r_m, and μ, and then specify the DSDs via eq. 10. Here the DSD considers the drop population over the entire collision volume V, but we can express the population in terms of a concentration simply dividing by V.

One further modification is made to specify the initial DSD. To simplify the initial SD sampling in the DSD tails and ensure a consistent representation of minimum and maximum initial drop size across the range of N_{SD} tested, the gamma distribution is truncated at minimum and maximum radii, r_{min} and r_{max} respectively. In the tests herein, we use r_{min} and r_{max} of 1 and 25 μm, respectively. SDs are initialized[1] from the DSD by dividing the size range into logarithmically spaced bins with a spacing of $\Delta_{lnr} = (\ln(r_{max}) - \ln(r_{min}))/(N_{SD}-1)$, similar to the initialization method in DP2017. The initial radius of the ith SD is then given recursively by $r_i = e^{(r_{i-1}+\Delta_{lnr})}$, where $r_1 = r_{min}$. Initial droplet mass is given by $m_i = 4\pi\rho_w r_i^3/3$ where ρ_w is the density of liquid water. A provisional initial multiplicity for the ith SD, M_i^*, is obtained from the discretized gamma DSD: $M_i^* = N_0 r_i^{\mu} e^{-\lambda r_i} \Delta r_i$, where $\Delta r_i = r_i - r_{i-1}$. To ensure consistency between the truncated DSD and N_{tot}, we uniformly scale SD multiplicities to ensure the total drop number in the collision volume (sum of the multiplicities of all SDs) is equal to N_{tot}. The final adjusted multiplicity for each ith SD, M_i, is therefore calculated as $M_i = M_i^* N_{tot} / \left(\sum_{i=1}^{N_{SD}} M_i^* \right)$.

[1]This method differs somewhat from the SD initialization in the LES which samples stochastically in logarithmic space over a range of aerosol sizes (see section 4a). This was done in the box simulations to eliminate initial condition variability and to ensure consistency in sampling across the range of initial drop sizes as N_{SD} is varied.

In the box simulations presented herein, we use $N_{tot} = 10^{11}$ and $V = 10^3$ m^3 (typical of the total drop number and volume of a LES grid cell) and $r_m = 12$ μm. There is a dependence on the initial r_m, with larger r_m yielding faster coalescence growth, but differences among the methods and sensitivity to N_{SD} are qualitatively consistent. For each model configuration, a range of N_{SD} is tested: 32, 64, 128, 256, 512, 1024, 2048, 4096, 8192. The time step $\Delta t = 1$ sec except for a set of sensitivity tests with the Δt reduced to 0.1 sec or increased to 10 sec discussed in the Appendix. All simulations apply the multiple coalescence approach from Shima et al. (2009) to account for P^*_{ij} or $P'_{ij} > 1$ (see also section 2). The simulation time is 3000 sec.

For the coalescence methods that incorporate some elements of stochasticity (all methods except AIM and dSDM), we run ensembles for each configuration of the box model. Each simulation in an ensemble is a different realization generated by applying different random number seeds for stochastic linear sampling of drop pairs and/or the stochastic Monte Carlo approach for coalescence. Using random number generators with a small cycle length can lead to degraded performance with super-particle microphysics (Unterstrasser et al. 2017). The random number intrinsic used here generates a 46 bit lagged Fibonacci pseudo-random sequence. The period of this generator is $\left(2^{17} - 1\right) 2^{45}$, much greater than the total number of random numbers drawn in our ensembles. For SDM, LSdSDM, and LSAIM we use 50 ensemble members. For fSDM, we use 20 ensemble members. Halving the number of members has little impacts on results and does not affect our conclusions.

b. Box model results

1) Drop size distribution analysis

Coalescence growth leads to a substantial shift of the initial DSD to larger drop sizes over time in all of the box simulations. However, there is considerable spread in the evolution of DSD shape using the different coalescence methods and at different values of N_{SD}. This is seen by comparing DSDs (ensemble mean ±1 standard deviation) at the time when 10% of total liquid mass is present in drops with radius ≥ 40 μm, t_{10} (Fig. 2). (Note that t_{10} itself also varies among simulations as described below.) SDM and fSDM produce broader DSD tails reaching r ~100 to 300 μm (Fig. 2a-f). The DSDs produced by LSdSDM at time t_{10} vary with N_{SD}, with a prominent right shoulder of the DSD and drops having $r > 100$ μm for $N_{SD} \geq 1024$, but with a maximum r of only

about 50 μm for N_{SD} = 128 (Fig. 2g-i). LSAIM retains the population of small drops similarly to SDM and fSDM, but produces a narrow second mode of larger drops with $50 < r < 100$ μm distinct from the main smaller mode (Fig. 2j-l). This larger mode is robust and occurs in all simulations using LSAIM. AIM and dSDM, which neglect statistical fluctuations in coalescence, have difficulty producing large drops. These methods produce a high concentration of medium size drops ($30 < r < 60$ μm) but no large drops; the maximum r is only 40-60 μm at time t_{10} over the range of N_{SD} in Fig. 2m-r. This result indicates how stochastic fluctuations in coalescence growth – whether by stochastic linear sampling of SD collision pairs or Monte Carlo all-or-nothing coalescence – are critical for producing large drops quickly. For all N_{SD}, the mean DSDs using dSDM and LSdSDM are relatively narrow with few drops of $r < 5$ μm, in contrast to the other coalescence methods. This occurs because fractional coalescence in dSDM and LSdSDM leads to growth of j drops when $M_i > M_j$ and $m_i > m_j$, which is generally the case for drops with $r < 5$ μm colliding with larger drops here. This is in contrast to the fractional coalescence in AIM and LSAIM which always grows larger drops in the SD pair regardless of which SD has a larger multiplicity (see the schematic diagram in Fig. 1).

2) Mean and variability of rain initiation time

Rain initiation in the box simulations is quantified by t_{10} following DP2017. Figure 3 presents ensemble mean $\overline{t_{10}}$ (where overbar denotes ensemble mean) for SDM, fSDM, dSDM, LSdSDM, LSAIM, and AIM over the range of N_{SD} from 32 to 8192. Note that AIM and dSDM are fully deterministic, so their "ensembles" consist of only a single simulation and $\overline{t_{10}}$ is simply the t_{10} from this simulation.

There is a decrease in $\overline{t_{10}}$ with increasing N_{SD} from 32 to ~256 in all ensembles except dSDM. This is consistent with DP2017, who showed similar behavior for SDM but with a different initial DSD (inverse exponential in mass rather than number). The methods with no stochastic variability (AIM and dSDM) – that is, using fractional coalescence and full sampling of SD coalescence pairs – produce the largest $\overline{t_{10}}$, except at $N_{SD} \leq 64$. This suggests the importance of stochastic coalescence variability in driving the growth of large drops using Lagrangian particle-based microphysics. Linear sampling of SD coalescence pairs plays an important role at small N_{SD} (≤ 256), with fSDM (using full sampling of coalescence pairs) giving larger $\overline{t_{10}}$ compared to SDM (using linear

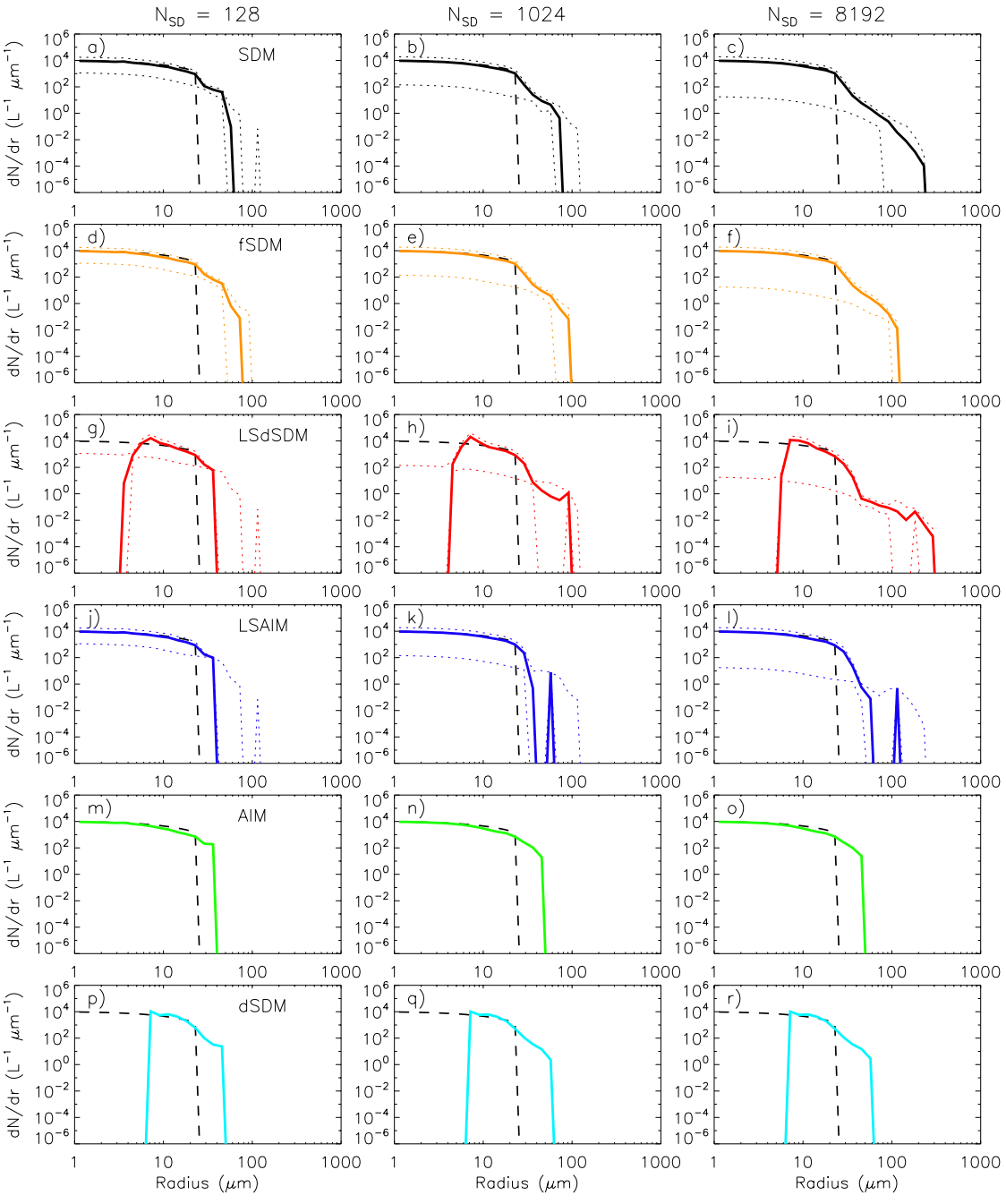

FIG. 2. DSDs from the box model simulations using various coalescence methods: a-c) SDM, d-f) fSDM, g-i) LSdSDM, j-l) LSAIM, m-0) AIM, p-r) dSDM. Results are shown for N_{SD} of 128 (left plots), 1024 (middle plots), and 8192 (right plots) at the time t_{10} of 10% condensate mass occurring in rain-sized drops (radius $\geq$ 40 μm) which varies among the simulations. Solid lines show the ensemble mean DSDs, dotted lines are the mean DSDs $\pm$1 standard deviation, and the dashed lines show the initial DSD.

sampling). It is notable that for $N_{SD} \leq 64$, fSDM produces similar $\overline{t_{10}}$ to the fully deterministic AIM and dSDM methods which also apply full sampling of SD pairs. Moreover, for N_{SD} less than about 512, all of the schemes with linear sampling of SD coalescence pairs produce similar $\overline{t_{10}}$. This occurs even though LSAIM and LSdSDM use fractional coalescence while SDM applies the Monte Carlo all-or-nothing approach. At larger N_{SD} (≥ 1024), the coalescence method (fractional versus all-or-nothing) is more important than sampling of SD coalescence pairs (linear versus full). That is, linear versus full sampling becomes less important with increasing N_{SD} as the total number of SD coalescence pairs increases. This explains why $\overline{t_{10}}$ values decrease for LSAIM and LSdSDM at $N_{SD} < 256$, but increase at larger N_{SD} and approach those from AIM and dSDM which apply full sampling of SD pairs. Similarly, fSDM approaches SDM at large N_{SD}, and they give similar $\overline{t_{10}}$ for $N_{SD} \geq 2048$.

Both SDM and fSDM are nearly converged with regard to N_{SD}, with less than 3% change over a range of N_{SD} from 2048 to 8192. AIM and dSDM converge at a smaller N_{SD}, with less than 2% change over a range of N_{SD} from 512 to 8192. However, they converge to $\overline{t_{10}}$ values nearly twice those from fSDM and SDM. Despite differences in how coalescence is treated between AIM and dSDM when $M_i > M_j$ and $m_i > m_j$ for an i, j SD coalescence pair (see section 2 and Fig. 1), they produce similar overall behavior with regard to $\overline{t_{10}}$. LSAIM and LSdSDM also give similar results to one another. These results suggest that differences in how collector and collectee SDs are defined using the fractional coalescence approaches in AIM and dSDM have little impact overall on rain initiation, though there is a large impact on the DSDs at small drop sizes as described below.

Figure 4 shows results for ensemble variability of rain initiation over the range of N_{SD}. This is quantified by the ensemble relative standard deviation of t_{10}, $\sigma_{t10}/\overline{t_{10}}$ where σ_{t10} is the ensemble standard deviation of t_{10}. Results for AIM and dSDM are not shown since they are fully deterministic and thus give $\sigma_{t10}/\overline{t_{10}} = 0$. As expected, LSAIM and LSdSDM, in which variability is only introduced by the stochastic linear sampling of SD coalescence pairs, produce $\sigma_{t10}/\overline{t_{10}}$ similar to one another but smaller than SDM by up to an order of magnitude, particularly for small N_{SD} (< 512). Besides the reduced variability overall, $\sigma_{t10}/\overline{t_{10}}$ is fairly constant with N_{SD} for LSAIM and LSdSDM. In contrast, SDM and fSDM give a consistent decrease of $\sigma_{t10}/\overline{t_{10}}$ for increasing N_{SD} for N_{SD} greater than about 128-256 (black and orange lines in Fig. 4). This is expected given

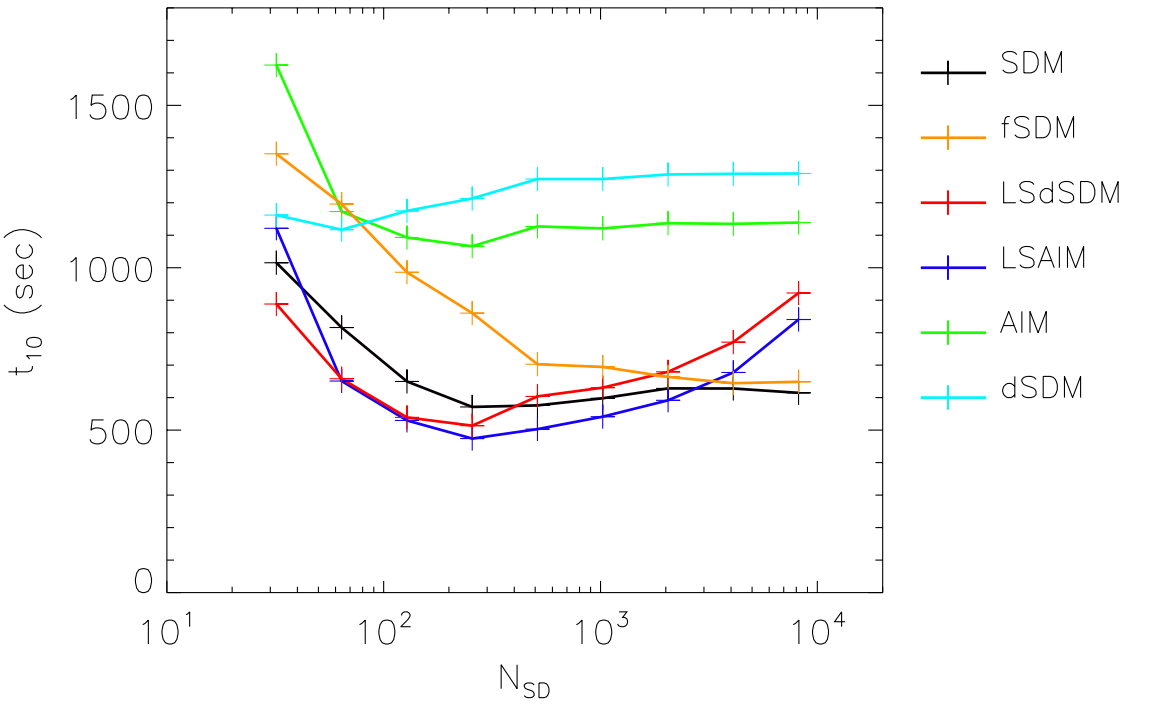

FIG. 3. Ensemble mean rain initiation time t_{10}, when 10% of condensate mass occurs as rain-size drops (radius ≥ 40 μm), from the box simulations as a function of N_{SD} for the various coalescence methods as labeled.

that variance in number of coalescence events scales with SD multiplicity using SDM (see section 2), and multiplicity uniformly decreases as N_{SD} increases with our SD initialization method. The additional variability from stochastic linear sampling of SD pairs in SDM compared to full sampling in fSDM leads to somewhat greater $\sigma_{t10}/\overline{t_{10}}$ in SDM, but the differences are small (less than a factor of 2 in all instances). Overall, the slopes of the decrease in $\sigma_{t10}/\overline{t_{10}}$ for SDM and fSDM are similar for $N_{SD} \geq 256$ to the empirical relation from DP2017 given by $6N_{SD}^{-1/2}$ (dotted black line in Fig. 4). If we extrapolate the DP2017 relation to the total number of drops in the collision volume (10^{11}), this gives $\sigma_{t10}/\overline{t_{10}} \sim 10^{-5}$ (note that the maximum $N_{SD} = N_{tot} = 10^7$ in DP2017). This is 3-4 orders of magnitude smaller than any of the simulations except those from AIM and dSDM, which have no variability. This excessive variability, particularly in SDM and fSDM, is expected when multiplicity is large. As DP2017 noted, a low number of computational particles relative to N_{tot} (i.e., large multiplicity) introduces unrealistic correlations between droplet sizes which amplifies coalescence fluctuations (Bayewitz et al. 1974). Variability of rain evolution of

the box simulations is analyzed in more detail in the Appendix, as well as sensitivity of t_{10} to the model time step.

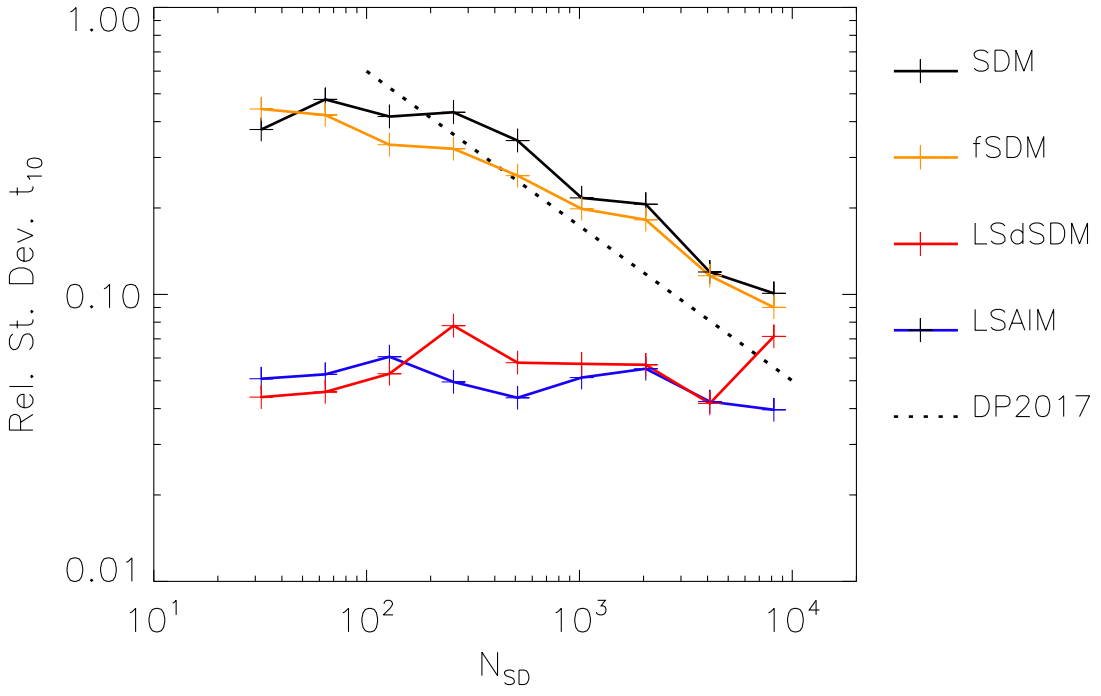

FIG. 4. As in Fig. 3 except for ensemble variability of t_{10} as quantified by relative standard deviation $\sigma_{t10}/\overline{t_{10}}$. The dotted line shows the empirical $\sigma_{t10}/\overline{t_{10}}$ versus N_{SD} relationship from DP2017.

4. Large-eddy simulations

a. Model description and experimental design

The LES are performed with the Cloud Model 1 (CM1, Bryan and Fritsch 2002), a nonhydrostatic model widely used to simulate atmospheric flows. We use the compressible dynamics option, with Klemp-Wilhelmson time splitting using a three-step Runge-Kutta time integration scheme and sub-time stepping for the acoustic modes. The basic model setup follows from Chandrakar et al. (2021) and Chandrakar et al. (2022). In this setup, which is similar to Lasher-Trapp et al. (2005), initial thermodynamic profiles are horizontally uniform except for random, small amplitude (±0.1 K) potential temperature (θ) perturbations applied throughout the domain. There is no initial wind shear. Horizontally uniform surface sensible and latent heat fluxes are applied during the first hour to spin up planetary boundary layer turbulence, after which Gaussian shaped fluxes are applied to

initiate cumulus congestus near the domain center. The model setup uses periodic lateral boundary conditions, a free slip upper boundary, and semi-slip lower boundary. The domain is 12.6×12.6 km^2 horizontally and 7.95 km vertically with a grid spacing of 75 m in each direction. A Rayleigh damper is applied above 7 km to mitigate wave reflection off the upper boundary. A fifth-order advection scheme is used for scalars and momentum. Subgrid-scale mixing is calculated using the prognostic turbulent kinetic energy option in CM1 (Deardorff 1980). Radiation is neglected. The time step is 2 sec with a 0.1 sec sub-time step for all microphysical processes using the Lagrangian scheme. Total simulation time is 135 min.

The Lagrangian microphysics scheme used here follows from that described by Shima et al. (2009). The implementation in CM1 is detailed in Chandrakar et al. (2021). Note that we refer to the microphysics scheme as a whole as the "Lagrangian scheme" rather than SDM, which is used instead herein to refer specifically to the Monte Carlo all-or-nothing coalescence method of Shima et al. (2009). The initial aerosol distribution follows from the Rain in Cumulus over the Ocean (RICO) model intercomparison of VanZanten et al. (2011), consisting of a bimodal lognormal distribution with a total concentration of 105 cm^{-3}. The SD initialization method sets minimum and maximum dry aerosol radii (here set to 0.01 and 5 μm, respectively), and applies uniform random sampling in the space of logarithmic dry radius. Multiplicity is then obtained from the specified aerosol distribution based on the radius of each SD. SDs are initially placed at random locations in each grid cell. The initial SD number in each grid cell is proportional to air density, with an average across all grid cells equal to the specified N_{SD}, following Chandrakar et al. (2021). Using this initialization method, similar to the box model, there is a wide range of multiplicities, from $O\left(10^2\right)$ to $O\left(10^{10}\right)$. Zmijewski et al. (2023) demonstrated that applying a constant multiplicity SD initialization gives poor convergence with N_{SD} and substantially less precipitation compared to an initialization method (somewhat different from ours) that also produces a wide range of multiplicities.

Drop condensation and evaporation are calculated from the resolved thermodynamic fields in CM1 at the scalar grid points. For simplicity the scalar thermodynamic fields are not interpolated to the SD locations. An implicit Euler scheme with Newton-Raphson iteration is used to solve the nonlinear condensation/evaporation equation including the solute and curvature terms. Additionally, Köhler theory is used for droplet activation and the growth/evaporation of hydrated aerosols.

SDs are transported by the resolved flow using the velocity field averaged over the acoustic substeps and linearly interpolated to the SD location. This approach uses a predictor-corrector method with horizontally periodic and reflective vertical boundary conditions. Inertial and drag terms are neglected except for gravitational settling. SDs are also transported via a subgrid-scale Lagrangian stochastic scheme given by eq. 1 in Chandrakar et al. (2021), which is similar to Weil et al. (2004). All ice microphysical processes and drop breakup are neglected for simplicity.

To separate variability associated with the flow from that driven directly by the microphysics, the piggybacking technique (e.g., Grabowski 2014; Grabowski and Jarecka 2015; Grabowski and Morrison 2016) is employed for most of the simulations. Here the driver variable set uses the Tel Aviv University (TAU) bin microphysics scheme (Tzivion et al. 1987; Feingold et al. 1988; Tzivion et al. 1989; Stevens et al. 1996) as applied in the simulations of Chandrakar et al. (2022). The piggybacker set uses Lagrangian microphysics with various configurations for collision-coalescence and N_{SD}. This allows for testing microphysical changes with the exact same flow field, meaning that the microphysical configurations with varying coalescence methods and N_{SD} can be compared without complications from variability in the flow. Details of the driver variable set are unimportant here; the main purpose is to generate a realistic flow field for testing the various Lagrangian microphysical configurations. We use the TAU scheme for this purpose primarily because it is computationally cheaper than the Lagrangian scheme, and it gives a flow field that is similar to simulations in which SDM feeds back to the dynamics rather than being piggybacked (see section 4c). Comparison of results using TAU versus SDM is beyond the scope of this paper, but examined in detail by Chandrakar et al. (2022) for the same case setup.

Because various aspects of stochastic variability are important, particularly the Monte Carlo all-or-nothing coalescence scheme used by SDM and stochastic linear sampling of SD pairs, ensembles are run for each microphysical configuration. For the generation of random numbers in the LES, we use the Mersenne Twister algorithm (Matsumoto and Nishimura 1998). A summary of the various LES microphysics ensembles is given in Table 2. We test only a limited number of configurations relative to the box model given the computational expense of LES. Two coalescence methods are tested – SDM and LSdSDM – to examine the impact of Monte Carlo all-or-nothing coalescence in SDM versus fractional coalescence in LSdSDM. These ensembles use an initial $N_{SD} = 128$

on average per grid cell, where we treat the SDM $N_{SD} = 128$ per grid cell[2] configuration as the "CONTROL" ensemble. Additional ensembles are run using SDM with N_{SD} of 32, 64, 256, and 512. To isolate variability introduced by the initial SD sampling and stochastic sub-grid scale SD transport, we also run an ensemble with LSdSDM and $N_{SD} = 128$ but with identical SD initialization (SD dry aerosol radius and position in the grid cell) among all ensemble members and with stochastic subgrid-scale SD transport neglected, referred to as mLSdSDM. In mLSdSDM, the only source of variability is the stochastic linear sampling of SD collision pairs. Additional ensembles to test the impacts of flow variability are described in section 4c.

TABLE 2. Summary of the LES microphysics ensembles. "SGS SD transport" indicates whether the sub-grid scale Lagrangian stochastic scheme of Chandrakar et al. (2021) is applied to SD transport. "Cost" is the mean total total number of core hours used for each simulation relative to the NSD32 simulations.

Name	Coalescence method	N_{SD}	SGS SD transport	Cost
NSD32	SDM	32	yes	1.00
NSD64	SDM	64	yes	1.45
CONTROL	SDM	128	yes	2.36
NSD256	SDM	256	yes	4.32
NSD512	SDM	512	yes	8.45
LSdSDM	LSdSDM	128	yes	2.45
mLSdSDM	LSdSDM	128	no	2.38

All ensembles include 8 members except for the $N_{SD} = 512$ ensemble which has only 5 members due to its high computational cost. The computational cost of all simulations measured by total core hour time relative to the NSD32 setup is shown in Table 2. As shown, the cost scales nearly linearly with the number of SDs for $N_{SD} \geq 128$, but is weaker than linear for $N_{SD} < 128$ since model components other than the microphysics contribute more to the cost when N_{SD} is small.

b. Results from LES microphysics ensembles

1) CONTROL SDM ENSEMBLE

All of the large-eddy simulations produce scattered shallow cumulus clouds after ~25 min. With the Gaussian-shaped surface flux forcing applied after 60 min (see section 4a), the main central congestus forms at ~85 min and grows upward. Subsidence around the cloud clears out the shallow

[2]Note that when describing the LES, N_{SD} will refer to the average SD number initialized per grid cell, and each cell is treated as a separate collision volume.

cumulus elsewhere in the domain. Cloud top reaches ~2.5 km by 100 min and ~3.5 km by 110 min. Thereafter it is between 3 and 4 km for the remainder of the simulations. Consistent with previous studies using a similar modeling setup (Chandrakar et al. 2021, 2022; Morrison et al. 2022), the main cloud flow comprises a series of large thermals that rise above cloud base, each with their own distinctive toroidal circulations. Domain maximum vertical velocities reach ~8 to 12 m s^{-1} and fluctuate over time as these cloud-scale thermals evolve. We emphasize that all piggybacking simulations with TAU as the dynamical driver have the exact same flow field.

Figure 5 shows vertical cross sections of vertical velocity (black contour lines), cloud water content L_c, and rain water content L_r (color contours) at three different times for a selected member of the CONTROL ensemble (SDM with $N_{SD} = 128$). In this simulation, maximum L_c values reach ~5 g kg^{-1} with rain water contents up to ~3 g m^{-3} (cloud and rain are separated based on drop radius of 40 μm). Rain is initiated aloft in the cloud by about 105 min, and it falls and reaches the surface by about 122 min. These general features are seen in all of the LES here, although rain initiation is substantially delayed in the LSdSDM and mLSdSDM ensembles (detailed later in this section). With the same flow field, the microphysical fields are quite similar among ensemble members. However, variability from stochastic microphysics (SD initialization, linear sampling of SD coalescence pairs, and the Monte Carlo coalescence scheme) introduces noticeable differences between members. These differences are quantified by the ensemble relative standard deviation of L_c and L_r, $\sigma_{Lc}/\overline{L_c}$ and $\sigma_{Lr}/\overline{L_r}$, respectively (where relative standard deviation is defined as the ensemble standard deviation divided by ensemble mean at each grid cell). Figure 6 shows vertical cross sections of the grid cell-by-cell $\sigma_{Lc}/\overline{L_c}$ and $\sigma_{Lr}/\overline{L_r}$. Values of $\sigma_{Lc}/\overline{L_c}$ in the cloud core are generally less than 0.2, increasing to 0.5 or greater along the cloud periphery where ensemble mean L_c values are small (Fig. 6a,c,e). Variability is much greater in the rain field, with $\sigma_{Lr}/\overline{L_r}$ generally between 0.5 and 2, but exceeding 2 along the periphery of the rain shaft (Fig. 6b,d,f). Values of $\sigma_{Lr}/\overline{L_r}$ are greatest when rain is first initiated, likely because of relatively small $\overline{L_r}$, and they decrease somewhat in the rain shaft core later.

Representative DSDs from the CONTROL ensemble are shown in Fig. 7a-c. DSDs in each LES grid were constructed from the SD data based on location and drop radius of each SD, with the data binned using a mass doubling grid (smallest bin with 1 μm radius). The figure presents DSDs at heights of 1500, 2625, and 3750 m and simulation time of 125 min (after the initiation

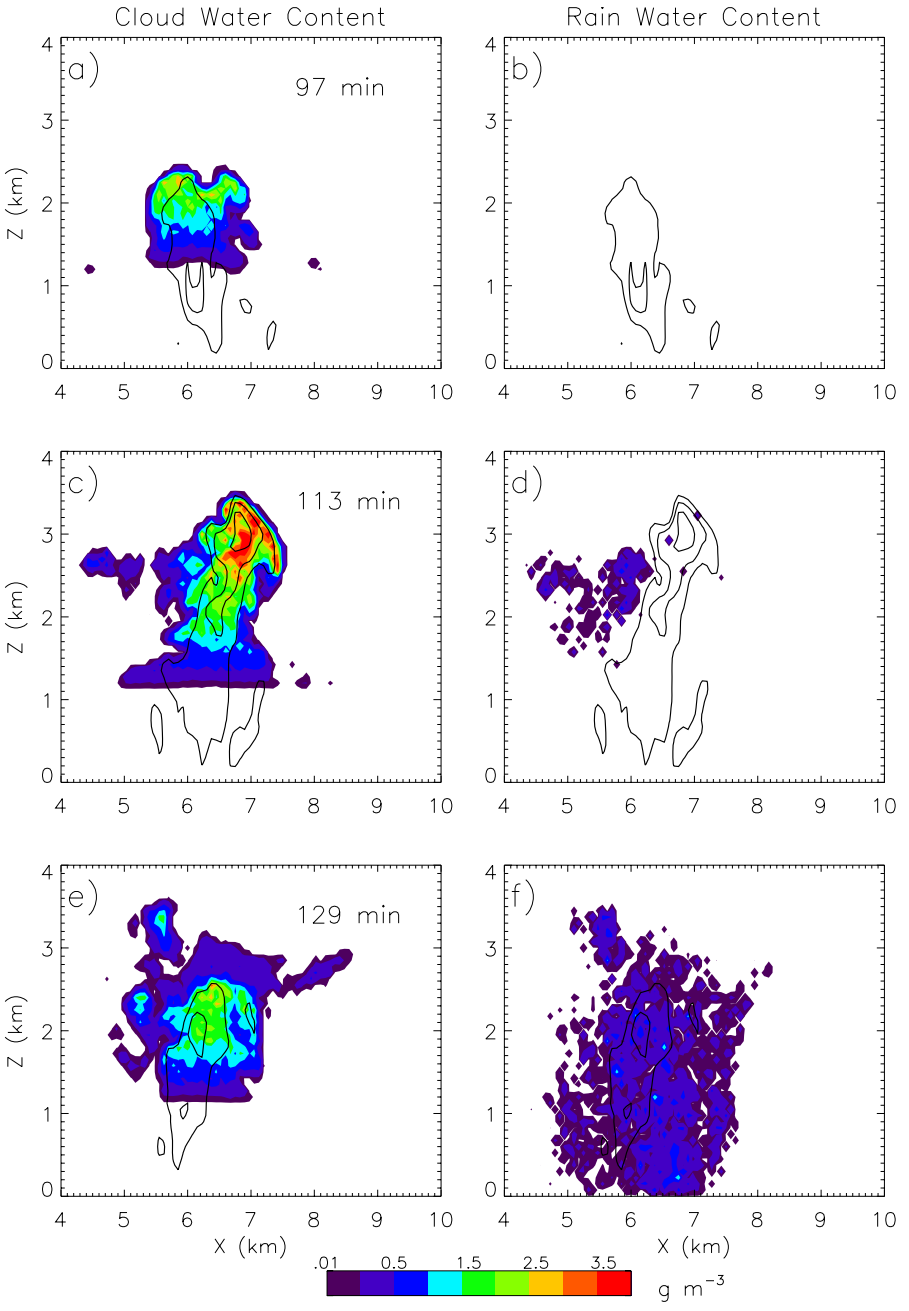

639 FIG. 5. Vertical cross sections in the x-z plane for one member of the CONTROL ensemble (SDM with
640 $N_{SD} = 128$) of a), c), e) cloud water content and b), d), f) rain water content at the three different times indicated.
641 Cloud and rain water contents are denoted by color contours and vertical air velocity by black contour lines starting
642 at 3 m s^{-1} and increasing every 3 m s^{-1}. Vertical cross sections are taken along the point with domain-maximum
643 vertical velocity at each time. Note only part of the domain is shown.

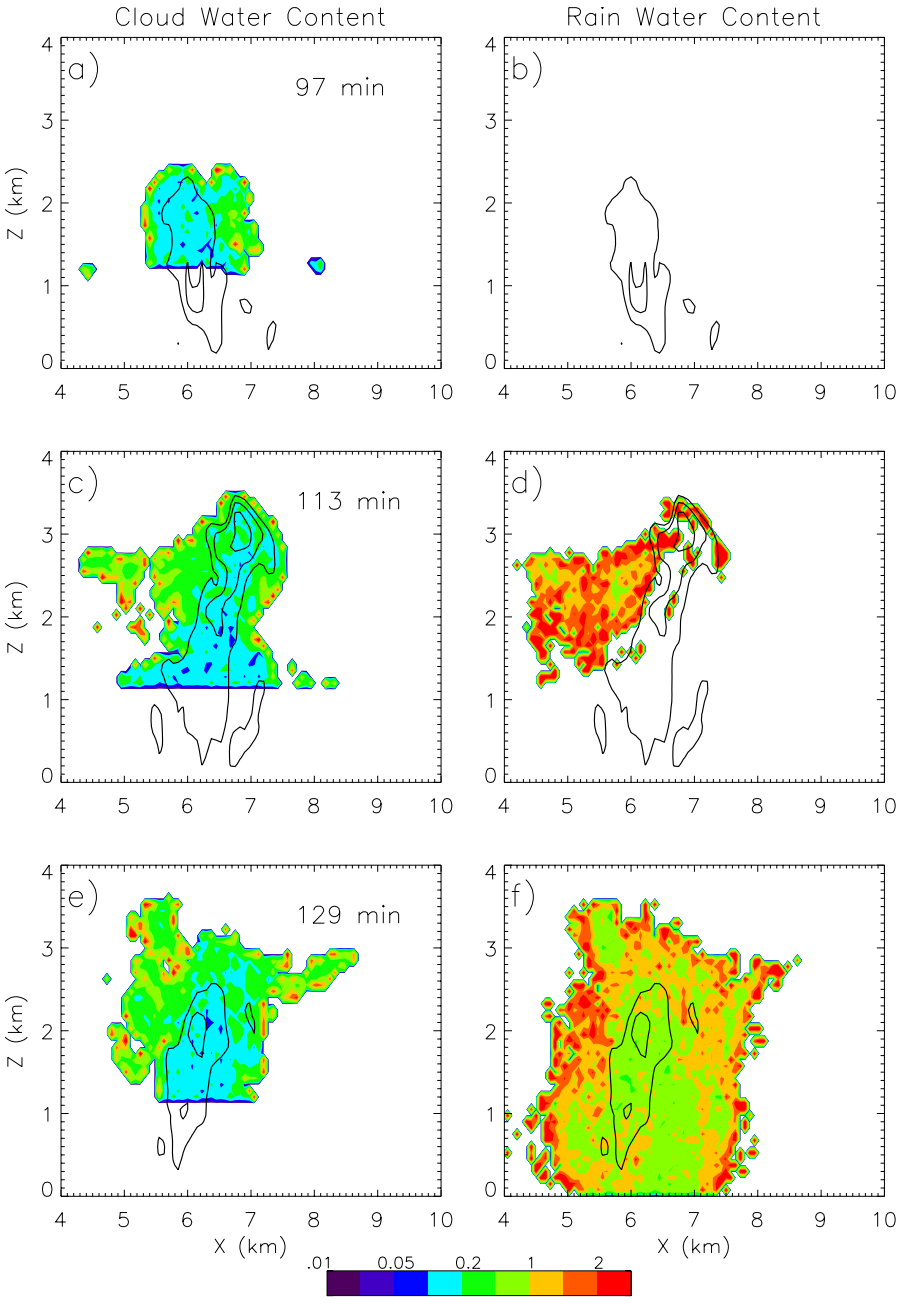

644 FIG. 6. As in Fig. 5 except for vertical cross sections of the CONTROL ensemble relative standard deviations
645 of cloud (left plots) and rain (right plots) water contents. Relative standard deviation (unitless) is calculated as
646 the cell-by-cell ensemble standard deviation divided by the ensemble mean. Note only part of the domain is
647 shown.

652 of substantial rain) from each member of the CONTROL ensemble (black lines) as well as the
653 ensemble mean DSDs (green lines). DSDs at each height from the individual ensemble members

are horizontally averaged over all grid points with total condensed water content $L_t \geq 0.1$ g m^{-3}. Near cloud top (3750 m), the DSDs have a shoulder of drizzle-sized drops with $40 < r < 400$ μm (Fig. 7c). These drops fall through the cloud and grow further by coalescence leading to a wider shoulder at 2625 m height with maximum drop radius near 1 mm (Fig. 7b). Just above cloud base (1500 m), a distinct bimodal structure is seen with a smaller cloud droplet mode at $r \sim 10$ μm and a larger rain mode with a broad peak at r between ~100-300 μm and maximum r near 2 mm (Fig. 7a). The concentration of small drops ($r < 10$ μm) is similar at all heights. This is caused by substantial secondary droplet activation above cloud base consistent with Chandrakar et al. (2021), who analyzed simulations using a similar cumulus congestus setup with CM1-SDM. They found about 25% of all drops in the cloud were formed by secondary activation above cloud base.

2) Sensitivity of SDM simulations to N_{SD}

Next we present ensemble results using SDM with N_{SD} varying from 32 to 512. Figure 8 shows timeseries of domain total cloud condensate mass, rain volume, and rain mass and horizontally-averaged cloud base rain flux F_{cb}[3] for the ensemble means and the means ±1 standard deviation. Here rain volume is defined as the total volume of all grid cells with rain water content ≥0.001 g m^{-3}. Cloud mass is very similar among the simulations which reflects the dynamical constraint using the piggybacking technique. Total rain mass decreases somewhat with increasing N_{SD}, by an average of 23% between 115 and 135 min increasing N_{SD} from 32 to 512, but with considerable ensemble spread as indicated by the ensemble standard deviations. In contrast, rain volume increases more substantially with increasing N_{SD}, by roughly a factor of 2 between $N_{SD} = 32$ and 512. These results give a picture of less frequent rain (smaller volume in the domain) with small N_{SD}, but much larger rain water content in grid cells with rain present. Horizontally-averaged F_{cb} also decreases somewhat as N_{SD} is increased from 32 to 512, by 21% when averaged over each ensemble from 115 and 135 min. These changes with N_{SD} are manifested by small differences in the ensemble mean DSDs (Fig. 7d-f). For instance, at lower and middle cloud levels the concentration of rain drops in the larger mode and DSD shoulder ($40 < r < 400$ μm) increases with a decrease in N_{SD} (Fig. 7d,e). At upper cloud levels the maximum drop size is somewhat larger (r ~800 μm) for $N_{SD} = 512$ compared to $N_{SD} = 32$ or 128 ($r \sim 500$ to 600 μm) (Fig. 7f).

[3]The analysis is focused on cloud base rain flux here since we are mainly concerned with initiation and early evolution of rain. Differences in surface rain flux across the LES ensembles are similar but with some delay in rain and smaller amounts overall than the cloud base rain flux.

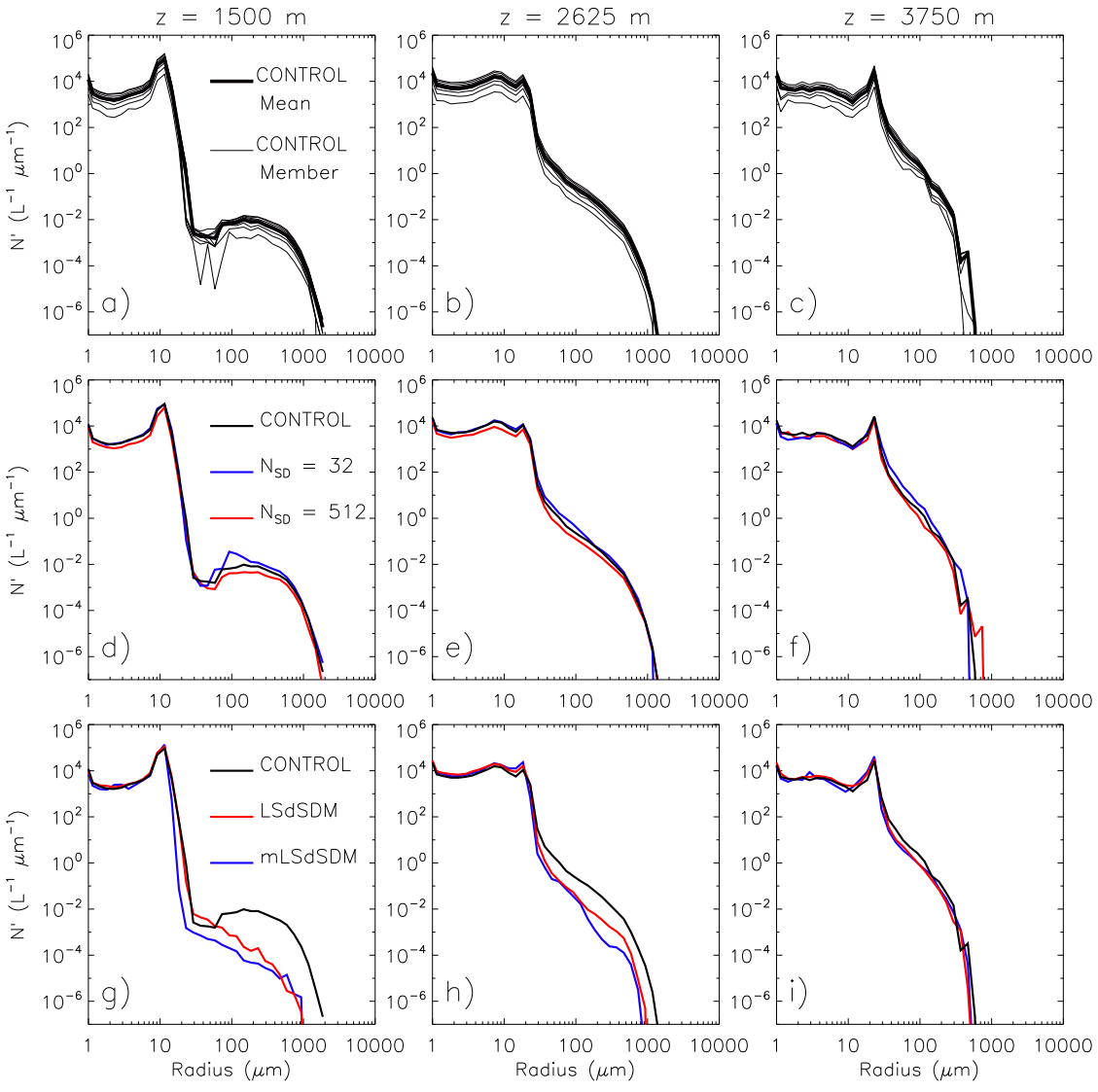

FIG. 7. Horizontally averaged DSDs from various ensembles at 125 min simulation time. a-c) DSDs from the CONTROL SDM ensemble with results from individual ensemble members shown by thin black lines and the ensemble mean by thick black lines. d-f) Ensemble mean DSDs from the CONTROL, $N_{SD} = 32$, and $N_{SD} = 512$ ensembles. g-i) Ensemble mean DSDs from the CONTROL, LSdSDM, and mLSdSDM ensembles. Left panels (a,d,g) show results at 1500 m height, middle panels (b,e,h) at 2625 m height, and right panels (c,f,i) at 3750 m height. Horizontal averaging includes all points with condensed water content ≥ 0.1 g m^{-3}.

A key result is that the timing of rain initiation is insensitive to N_{SD}; there are no consistent changes in rain initiation time among the SDM ensembles with varying N_{SD}, both as quantified by domain total rain mass and F_{cb}. Indeed, one of the $N_{SD} = 32$ ensemble members has the

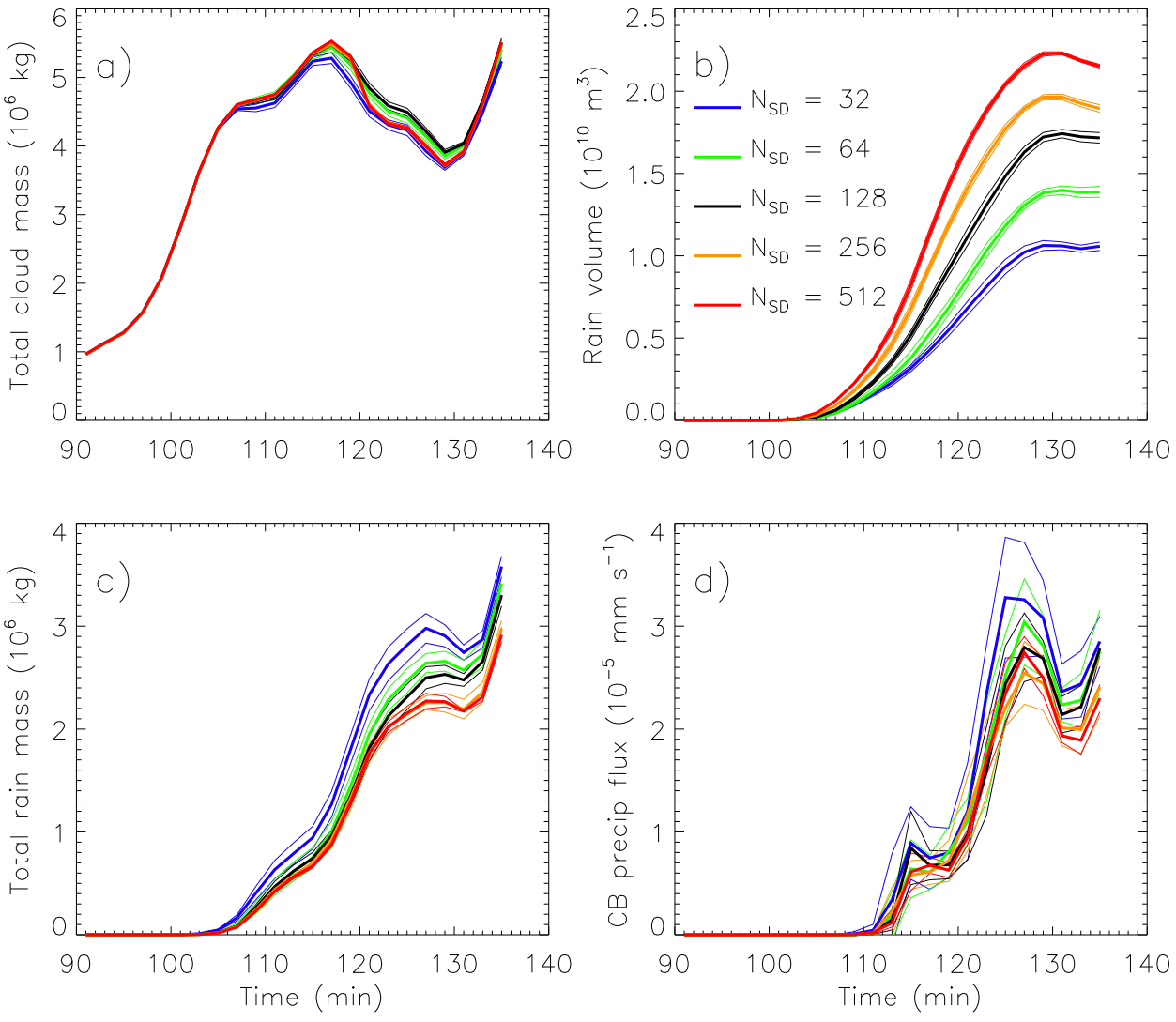

FIG. 8. Timeseries of domain total a) cloud mass, b) rain volume, and c) rain mass and d) horizontally-averaged cloud base (CB) rain flux from the SDM ensembles with varying N_{SD}. Thick lines show ensemble means and thin lines show ensemble means ±1 standard deviation.

earliest rain (quantified by the time when horizontally-averaged $F_{cb} \geq 10^{-6}$ mm s^{-1}) among all of these ensembles. This finding contrasts with the box model tests showing the ensemble mean rain initiation time $\overline{t_{10}}$ decreased by almost a factor of 2 as N_{SD} was increased from 32 to 512, but is consistent with overall rain initiation from the box model ensembles being controlled by their members that produced rain fastest (shown in Fig. A2). The LES can be considered as a large ensemble of separate collision volumes (only SDs within the same grid cell may possibly coalesce), with roughly 2×10^4 cloudy grid cells during the mature stage of the cloud. Although rain is slow to

develop *on average* in a collision volume using small N_{SD}, as demonstrated by the box model tests, large variability means that some LES grid cells initiate rain much faster than others. Large drops that happen to form by statistical fluctuations in some grid cells are transported to neighboring cells, particularly by sedimentation once drop fallspeed becomes significant (10's of cm s^{-1} or more). Thus, considering individual grid cells, delayed mean rain initiation but larger variability at low N_{SD} compensate so that rain is initiated overall from the cloud at a similar time as at high N_{SD} but in a smaller number of cells. As a consequence, although the timing of rain initiation is insensitive to N_{SD}, rain volume in the domain increases substantially as N_{SD} is increased.

Another important result is that the rain that does form at low N_{SD} is present in SDs with a relatively large multiplicity compared to rain SDs at high N_{SD}. This is a direct consequence of the inverse relation between N_{SD} and multiplicity, leading to greater correlation of coalescence growth among drops as N_{SD} is decreased. Thus, rain SDs at low N_{SD} tend to have a relatively large total mass (multiplicity times mass of each drop comprising the SD). For example, the average total mass and multiplicity of rain SDs ($r \geq 40$ μm) at 125 min are 16 and 28 times larger, respectively, for $N_{SD} = 32$ compared to 512. These SDs fall and collect additional mass by coalescence, explaining the large values of "in-rain" average L_r (including only grid cells with $L_r \geq 0.001$ g m^{-3}) when N_{SD} is small. Locally large L_r values compensate for lower rain fraction at small N_{SD} and the domain total rain mass and F_{cb} decrease slightly as N_{SD} is increased.

Although rain volume and in-rain water content do not converge as N_{SD} is increased from 32 to 512, nor ensemble variability in cloud and rain properties as discussed below, there is some evidence for convergence of the ensemble mean total rain mass and horizontally-averaged F_{cb}. The decrease in these quantities (averaged from 115 to 135 min) is only 0.7% for total rain mass and 1.0% for horizontally-averaged F_{cb} as N_{SD} is increased from 256 to 512, whereas the relative decrease is much larger for each doubling in N_{SD} from 32 to 256 (e.g., −8.1% for total rain mass and −7.1% for F_{cb} increasing N_{SD} from 128 to 256). Confirming if the LES are indeed practically converged at $N_{SD} = 256$ will require additional simulations with $N_{SD} > 512$, which is computationally intensive and left for future work.

As expected theoretically and consistent with the box model results, ensemble spread decreases as N_{SD} is increased. We quantify ensemble spread by the relative standard deviations of L_r, L_t, and the number-weighted mean drop radius $r_m \equiv \int rN'dr / \int N'dr$, calculated grid cell-by-cell across

each ensemble; these are denoted as $\sigma_{Lr}/\overline{L_r}$, $\sigma_{Lt}/\overline{L_t}$ and $\sigma_{rm}/\overline{r_m}$, respectively. Figure 9 shows timeseries of $\sigma_{Lr}/\overline{L_r}$, $\sigma_{Lt}/\overline{L_t}$ and $\sigma_{rm}/\overline{r_m}$ spatially averaged over all grid cells with ensemble mean $\overline{L_t} \geq 0.1$ g m^{-3} for $\sigma_{Lt}/\overline{L_t}$ and $\sigma_{rm}/\overline{r_m}$ and $\overline{L_r} \geq 0.1$ g m^{-3} for $\sigma_{Lr}/\overline{L_r}$. Results for each ensemble across the range of N_{SD} are shown in the figure. There is a monotonic decrease of spatially-averaged $\sigma_{Lt}/\overline{L_t}$, $\sigma_{rm}/\overline{r_m}$ and $\sigma_{Lr}/\overline{L_r}$ at all times as N_{SD} is increased. Spatially-averaged $\sigma_{Lt}/\overline{L_t}$ and $\sigma_{rm}/\overline{r_m}$ are small early in the simulations when DSD evolution is dominated by condensation but increase after substantial coalescence growth and initiation of rain. Given that rain mass is primarily generated via Monte Carlo coalescence in SDM whereas cloud mass is grown by condensation, it is not surprising that $\sigma_{Lt}/\overline{L_t} < \sigma_{Lr}/\overline{L_r}$ for these ensembles. The decrease in ensemble variability with each doubling of N_{SD} is similar over the range from 32 to 512, with no evidence for convergence. Spatial variability of L_r, L_t, and r_m, quantified by the relative standard deviation along horizontal slices through the cloud (cell-by-cell) for each ensemble member, also decreases with increasing N_{SD} (not shown) similar to the ensemble variability.

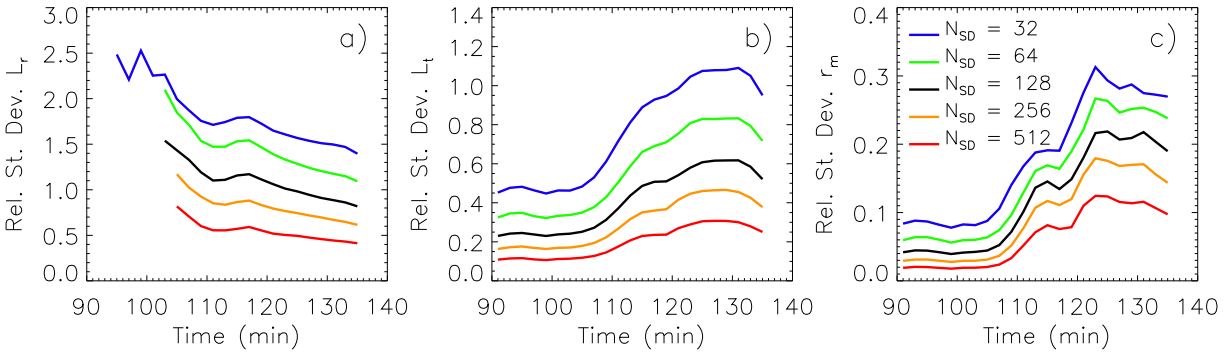

FIG. 9. Timeseries of ensemble relative standard deviations (unitless) of a) rain water content (L_r), b) total condensed water content (L_t), and c) number-weighted mean drop radius (r_m). Results are shown for the ensembles with varying N_{SD}. Ensemble standard deviations are calculated grid cell-by-cell and averaged spatially including points with ensemble mean $L_t \geq 0.1$ g m^{-3} for relative standard deviations of L_t and r_m and $L_r \geq 0.1$ g m^{-3} for relative standard deviation of L_r.

3) Comparison of stochastic all-or-nothing and fractional coalescence methods

To examine how stochastic coalescence fluctuations impact rain initiation further, we compare ensembles using either SDM (the CONTROL ensemble) or LSdSDM, both with $N_{SD} = 128$. Recall that these coalescence schemes solve the same equation set, but SDM uses a probabilistic "all-

or-nothing" Monte Carlo approach while LSdSDM uses a deterministic fractional coalescence approach that limits coalescence variability (see section 2). We also analyze the mLSdSDM ensemble, which is the same as LSdSDM but uses fixed SD initialization (all ensemble members employ the same initial SD sampling) and turns off sub-grid scale SD transport; the only source of variability in mLSdSDM is stochastic linear sampling of SD coalescence pairs.

Figure 10 shows timeseries of domain total cloud and rain masses, rain volume, and horizontally-averaged F_{cb} for LSdSDM and mLSdSDM in the same format as Fig. 8. A key result is that rain initiation is substantially delayed – by about 15-18 min – using LSdSDM compared to SDM. Differences in rain initiation time (again defined by horizontally-averaged $F_{cb} \geq 10^{-6}$ mm s^{-1}) between the CONTROL (SDM) and LSdSDM are well outside of the ensemble spread. These differences are reflected by DSDs (averaged for all points with $L_t \geq 0.1$ g m^{-3}) seen in Fig. 7g-i. Although the DSDs in CONTROL and LSdSDM are similar near cloud top (3750 m height), there are substantial differences lower in the cloud at 2635 m and especially at 1500 m. Specifically, the concentration of drops with $r > 50$ μm is 1-2 orders of magnitude smaller in LSdSDM than CONTROL. While a shoulder of rain sized drops is present in the mean LSdSDM DSD just above cloud base (1500 m), there is no distinct second mode of rain drops unlike in CONTROL.

These results indicate the critical role on warm rain initiation of coalescence fluctuations associated with the stochastic all-or-nothing approach in SDM compared to the fractional approach in LSdSDM. Delayed rain initiation using LSdSDM seemingly contradicts the box model tests in which LSdSDM and SDM produced similar ensemble mean rain initiation time for $N_{SD} = 128$ (see section 3b and Fig. 3). What explains this discrepancy? As shown by the box model tests, ensemble variability in rain initiation time is much smaller for LSdSDM compared to SDM. LES grid cells that happen to have faster drop growth owing to statistical fluctuations greatly accelerate overall rain production in the cloud using SDM, where these embryo rain drops are subsequently transported to neighboring grid cells leading to more widespread rain generation. In contrast, the fractional coalescence approach in LSdSDM results in fewer grid cells that initiate rain drop embryos (hence the very small rain volume, see Fig. 10b), even though the *mean* rain initiation time for an ensemble of collision volumes is similar between LSdSDM and SDM as shown by the box model simulations at $N_{SD} = 128$.

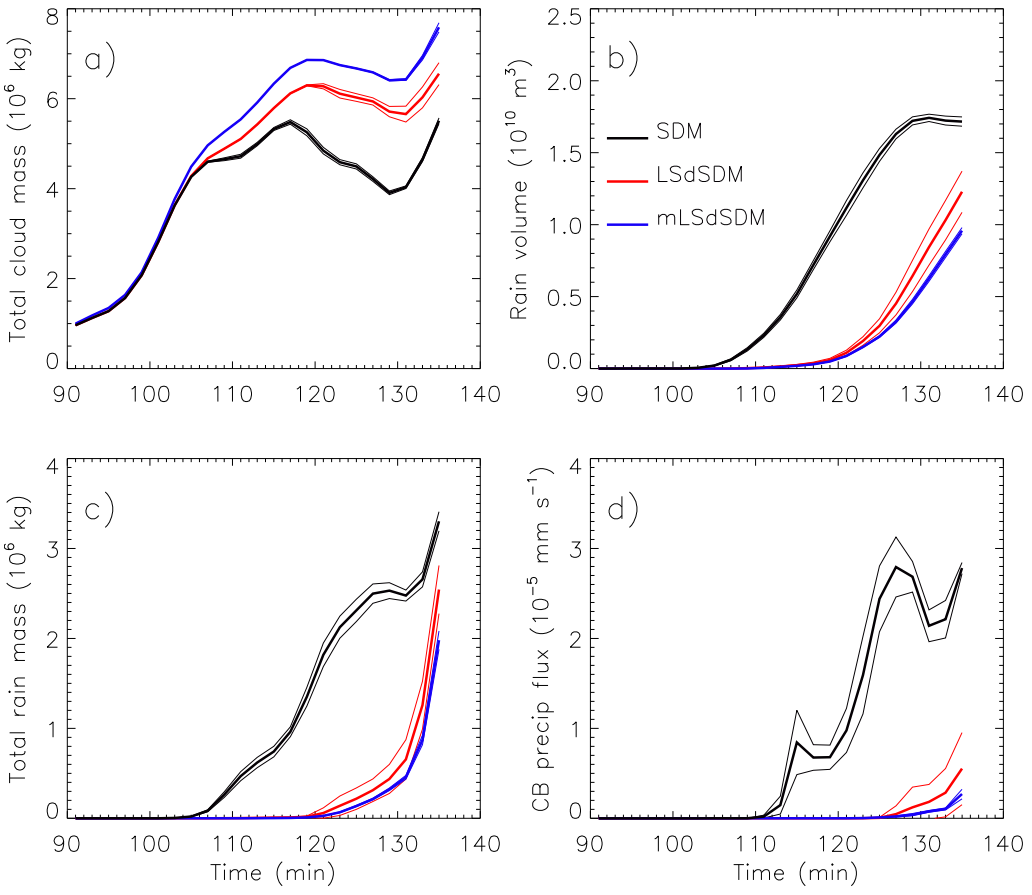

FIG. 10. As in Fig. 8 except for the CONTROL (SDM), LSdSDM, and mLSdSDM ensembles with $N_{SD} = 128$.

A comparison of LSdSDM and mLSdSDM in Fig. 10 shows that they produce similar ensemble mean cloud and rain properties, with both substantially delaying rain initiation compared to SDM (blue and red lines versus black lines). LSdSDM appears to produce slightly more rain on average than mLSdSDM (greater domain total rain mass and rain fraction as well as domain-mean cloud base rain flux), which might indicate the role of drop fluctuations from SD initialization and subgrid-scale transport in enhancing coalescence. However, differences in the LSdSDM and mLSdSDM ensemble means are within the spread of these ensemble. A similar story holds for the ensemble and horizontally-averaged DSDs (Fig. 7g-i), with similar DSD shapes but mLSdSDM having somewhat fewer raindrops with $\sim 40 < r < 400$ μm than LSdSDM.

An interesting feature is that despite having little variability in DSD evolution before rain initiation using LSdSDM, there is large variability in rain properties (particularly horizontally-averaged F_{cb}) after rain is initiated. The spread in these quantities by 135 min in LSdSDM is even larger than

in the CONTROL (SDM) ensemble, seen by the ensemble standard deviations in Fig. 10b-d. Because all ensemble members have the same flow field, there are only three possible sources of ensemble variability in LSdSDM: 1) stochastic linear sampling of SD coalescence pairs; 2) random sampling for SD initialization (size and location of SDs within a grid cell); 3) sub-grid scale SD transport which involves solving a Lagrangian stochastic differential equation (see section 4a). The mLSdSDM ensemble, in which the second and third sources of variability above are neglected, helps to address this question. It is clear from Fig. 10 that ensemble variability for mLSdSDM is greatly reduced compared to LSdSDM. We therefore conclude that the large variability in the LSdSDM ensemble after rain is initiated is caused mainly by initial SD sampling and/or subgrid scale transport, and stochastic sampling of SD coalescence pairs contributes much less to variability.

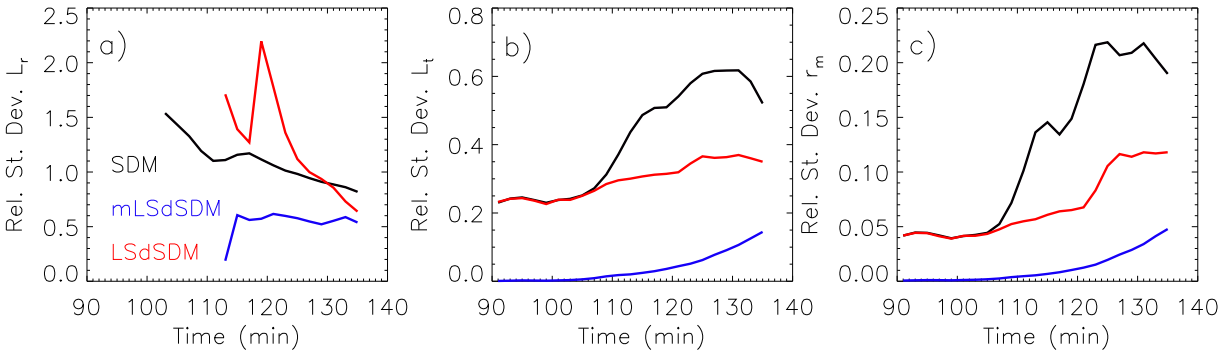

FIG. 11. As in Fig. 9 except the CONTROL (SDM), LSdSDM, and mLSdSDM ensembles.

Variability of the CONTROL, LSdSDM, and mLSdSDM ensembles is further quantified by spatially-averaged grid cell-by-cell relative standard deviations of L_r, L_t, and r_m. Figure 11 shows timeseries of the relative standard deviations for these ensembles calculated in the same way as Fig. 9. Consistent with the results discussed above, ensemble variability is greatly reduced for mLSdSDM, particularly earlier in the simulations for L_t and r_m. This is expected given that SD initialization and especially stochastic subgrid-scale transport dominate ensemble variability in CONTROL and LSdSDM when growth is predominately by condensation, and these sources of variability are excluded in the mLSdSDM ensemble. LSdSDM has generally larger $\sigma_{Lr}/\overline{L_r}$ than CONTROL once rain is initiated consistent with Fig. 10. Large ensemble rain variability in LSdSDM is explained by the fact that rain is initiated in relatively few grid cells (i.e., small rain fraction in the domain) compared to the CONTROL ensemble. As a consequence, there are relatively large statistical fluctuations in rain properties (including L_r) driven by variability from

SD initialization and subgrid scale transport considering only cells with $L_r \geq 0.1$ g m^{-3}. This also explains why $\sigma_{Lr}/\overline{L_r}$ decreases over time (Fig. 11a) as the number of cells with rain increases. In contrast, ensemble variability of L_t and r_m, as quantified by $\sigma_{Lt}/\overline{L_t}$ and $\sigma_{rm}/\overline{r_m}$ considering all grid points with condensed water ($\overline{L_t} \geq 0.1$ g m^{-3}), is larger in CONTROL than LSdSDM over the entire simulation period by up to a factor of 2 (Fig. 11b,c). This is consistent with much greater coalescence variability using the Monte Carlo all-or-nothing scheme in SDM compared to the fractional approach in LSdSDM, and overall reduced microphysical variability in LSdSDM.

TABLE 3. Summary of the LES flow ensembles. "Initial θ" indicates whether random initial θ perturbations are the same or different for all ensemble members.

Name	Coalescence method	N_{SD}	Piggybacking	Initial θ
TFLOW	SDM	128	yes	different
SFLOWIN	SDM	128	no	different
SFLOW	SDM	128	no	same

c. Variability from different flow realizations versus stochastic microphysics

Three ensembles are performed to examine impacts of flow variability (see Table 3). The first one applies different seeds for random, small-amplitude perturbations of the initial θ field which generates diverging flow with the TAU dynamical driver across the ensemble (TFLOW). In this ensemble, SDM is the piggybacker. The second flow ensemble also applies different seeds for the initial θ perturbations, but instead of applying piggybacking it couples SDM directly to the flow in a two-way feedback (SFLOWIN). The third flow ensemble also has a two-way coupling of SDM to the dynamics, like SFLOWIN, but uses the same random number seed for the initial θ perturbations for all members (SFLOW). Thus, all members in the SFLOW ensemble have identical initial conditions but their flows diverge over time owing to microphysics-dynamics feedback. All three ensembles use SDM with $N_{SD} = 128$.

Figure 12 shows timeseries of domain total cloud water and rain water masses, rain volume, and horizontally-averaged F_{cb} in a similar format as Figs. 8 and 10. An obvious difference compared to the CONTROL ensemble with fixed dynamics via piggybacking is the much larger ensemble spread in all quantities. For example, the mean ensemble relative standard deviation of horizontally-averaged F_{cb} between 115 and 135 min is approximately 3 times larger for the TFLOW, SFLOWIN,

and SFLOW (0.52, 0.51, and 0.46 respectively) ensembles compared to the CONTROL (0.17). This is similar to Zmijewski et al. (2023), who found ~4 times larger relative standard deviation of surface rain accumulation in dynamic ensembles with perturbed initial conditions compared to microphysical ensembles using SDM with piggybacking. The ensemble spread here is similar among TFLOW, SFLOWIN, and SFLOW, particularly after ~100 min. This reflects the rapid growth of small amplitude perturbations in turbulent flow regardless of the perturbation source: random initial θ perturbations in TFLOW and SFLOWIN or random microphysical perturbations that feed back to the dynamics in SFLOW. That said, SFLOW has less ensemble spread before ~100 min, which likely reflects reduced microphysical variability prior to the onset of significant coalescence. Ensemble mean cloud and rain quantities (Fig. 12d,h,l,p) are similar for CONTROL, TFLOW, SFLOWIN, and SFLOW, well within the spread of the latter three ensembles. This indicates rather small ensemble-averaged differences whether TAU or SDM drives the dynamics.

5. Summary, discussion and conclusions

In this study, we examined impacts of different coalescence methods on microphysical evolution using Lagrangian super-particle microphysics in a box model and in LES of a cumulus congestus cloud. Besides the standard Monte Carlo all-or-nothing SDM (Shima et al. 2009) and deterministic fractional AIM (Riechelmann et al. 2012) approaches, a deterministic version of SDM (dSDM) was proposed and tested to further understand the impacts of coalescence variability in Lagrangian microphysics schemes. dSDM is identical to SDM except that it coalesces a fraction of drops in each SD pair based on the coalescence probability and distributes the coalesced mass evenly among all drops in the collector SD (i.e., fractional coalescence), in contrast to the all-or-nothing Monte Carlo approach in SDM. Because the number of coalescence events is always equal to the expected value at each time step in dSDM, and because all drops in the collector SD grow at the same rate, similar to AIM, the representation of lucky drops in dSDM is inherently limited compared to SDM. We used "piggybacking" with the LES to separate impacts of microphysical variability from flow variability. Additional ensembles with different flow realizations were performed to quantify ensemble spread from dynamical versus (direct) microphysical variability.

We highlight the following main results of the study in addressing the four science questions posed in the introduction:

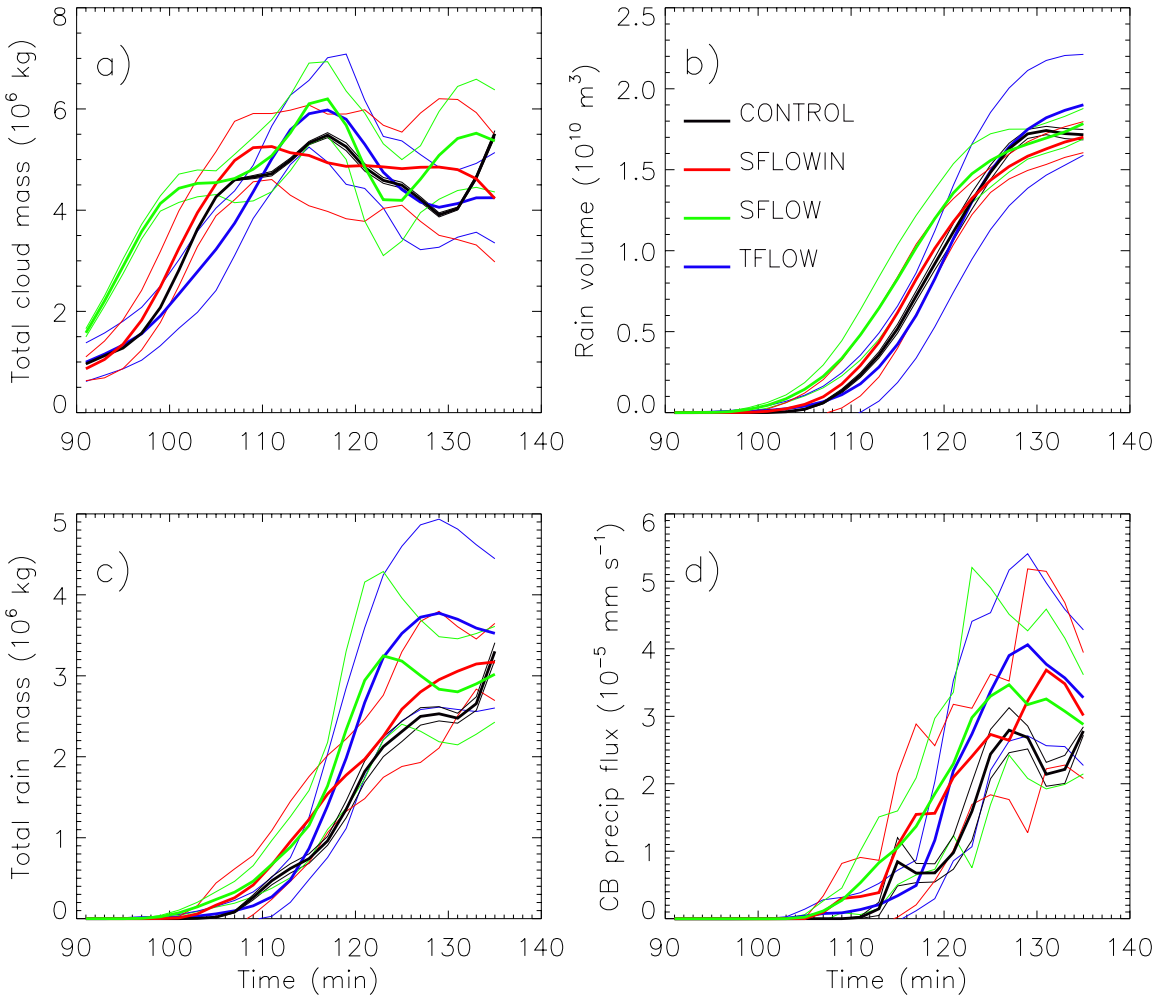

853 FIG. 12. As in Fig. 8 except for the CONTROL, TFLOW, SFLOWIN, and SFLOLW ensembles with flow
854 variability.

872 • Stochastic fluctuations using the all-or-nothing approach in SDM led to much faster rain
873 production in both the box model and LES (by ~10 min or more) compared to using the
874 fractional coalescence approaches in AIM and dSDM.

875 • Rain initiation averaged over many realizations of the box model was much slower ($\overline{t_{10}}$
876 increasing by ~60%) when N_{SD} was decreased from 256 to 32 using SDM, with less sensitivity
877 for $N_{SD} \geq 256$. AIM and dSDM overall showed little sensitivity of rain initiation to N_{SD} in
878 the box model.

- Sensitivity of rain initiation to N_{SD} differed markedly between the box model and LES. In contrast to the delay of rain initiation using SDM in an ensemble of box model simulations at $N_{SD} < 256$, the timing of rain initiation was insensitive to N_{SD} in the LES. This occurred because of interaction between the LES grid boxes, each acting as a separate collision volume. Variability across the LES grid boxes led to some cells quickly initiating rain even at low N_{SD}, and this determined the overall timing of rain initiation from the cloud.

- The ensemble spread of various cloud and rain properties (e.g., domain total cloud and rain mass, horizontally-averaged cloud base rain flux F_{cb}) was much greater for the flow ensembles than the microphysical ensembles with piggybacking (and thus fixed flow), by roughly a factor of 3. Thus, flow variability associated with initial condition perturbations and microphysics-dynamics interactions dominates variability driven by stochastic coalescence fluctuations in SDM.

The last item above is consistent with Zmijewski et al. (2023), who similarly showed much larger cloud and precipitation variability resulting from different flow realizations with small perturbations to initial conditions. We demonstrated that this conclusion holds even with fixed initial conditions when microphysical variability is allowed to feed back to the dynamics. Thus, in lieu of large ensembles that may not be practical from a computational standpoint, it is critical to constrain dynamical variability in order to isolate the direct impacts of microphysical variability and test for convergence of numerical methods. Moreover, we conclude that the well-known excessive coalescence variability in SDM is unlikely to be important in practice for LES given it is overwhelmed by flow variability when the microphysics is allowed to feed back to the dynamics. This mitigates a concern using SDM raised in some previous papers (e.g. Unterstrasser et al. 2017), and implies that ensemble sizes needed to obtain statistically robust results should be determined primarily by flow variability rather than the microphysics.

Although AIM and dSDM were fairly insensitive to N_{SD} in the box model tests, they converged to solutions with a factor of ~2 slower rain production compared to SDM. Similarly, LSAIM and LSdSDM approached AIM and dSDM as N_{SD} was increased above 256 and linear versus full sampling of SD coalescence pairs became less important. Although SDM converged at a larger N_{SD} than AIM or dSDM, it is consistent with the primitive model (which represents every particle explicitly); as N_{SD} approaches the total number of physical drops in a system SDM

becomes analogous to the primitive model. We conclude, therefore, that schemes using the fractional coalescence approach (including AIM and dSDM) converge to incorrect solutions. This occurs because the fractional coalescence approach gives an implied number of coalescence events different from the actual number as detailed in section 2e, and this problem would need to be resolved for deterministic particle-based models using the fractional approach to be viable.

The multiplicity and total mass of rain SDs in the LES scaled approximately with N_{SD}, and this compensated for a smaller number of grid cells with rain at low N_{SD} to give similar domain total rain mass and horizontally-averaged F_{cb} as N_{SD} was increased. There was a $\sim 20\%$ decrease in total rain mass and horizontally-averaged F_{cb} with an increase in N_{SD} from 32 to 256, but only a $\leq 1\%$ decrease as N_{SD} was increased from 256 to 512. Thus, there is some evidence of convergence in cloud and rain properties at $N_{SD} \geq 256$ in the LES, and these results provide practical guidance using SDM in 3D cloud models. However, additional testing with $N_{SD} > 512$ should be done to confirm convergence at $N_{SD} \geq 256$. Moreover, we emphasize that convergence may occur at different values of N_{SD} with changes to the model grid spacing. Because SDs are transported across grid cells in the LES, the effective number of SDs is much higher than in independent box model simulations for the same N_{SD}. Moreover, inherently more SDs will be transported across grid cells per unit time as the grid spacing is decreased. Thus, we expect that convergence may occur at smaller values of N_{SD} with a reduction in grid spacing. This could not be easily tested using the piggybacking framework employed here because different grid spacings will lead to different flow realizations (and possibly systematic changes to the flow). However, sensitivity to N_{SD} across different grid spacings is an important topic that should be investigated in future work.

Our finding of substantial differences in rain generation in the box model versus LES is broadly consistent with Unterstrasser et al. (2020) and Zmijewski et al. (2023). However, our results differ in some important details. Although we found a monotonic decrease in rain amount as N_{SD} was increased up to 512, Zmijewski et al. (2023) observed a decrease followed by an increase, with a minimum for N_{SD} around 100 (1000 in one case). As noted above, limited sensitivity of rain to N_{SD} in our LES was explained by compensation between the number of cells with rain and local rain water content owing to differences in rain SD multiplicity with changes to N_{SD}. Because SD multiplicity is strongly influenced by initialization of SDs, we speculate that differences in SD initialization may have contributed at least in part to lower sensitivity of rain

to N_{SD} here compared to the simulations of Zmijewski et al. (2023), besides different dynamical frameworks (e.g., 2D versus 3D). Sensitivity of rain properties to SD initialization may also help to explain the spread of box and 1D model results found by (Hill et al. 2023) for different SDM implementations with the same N_{SD} and collection kernel. Our results generally do not support the hypothesis in Zmijewski et al. (2023) that reduced coalescence variability and smaller grid cell-to-cell microphysical differences with increasing N_{SD} lead to more precipitation, at least for $N_{SD} \leq 512$. In our simulations, there was a reduction of both spatial variability and cell-by-cell ensemble variability of various microphysical quantities (L_t, L_r, D_m) as N_{SD} was increased, accompanied by a small *decrease* in horizontally-averaged F_{cb}.

Reduced microphysical variability using LSdSDM (dSDM with linear sampling of SD coalescence pairs) compared to SDM led to a substantial delay in rain initiation (by ~15-18 min) in the LES and much smaller horizontally-averaged F_{cb}. We conclude that the Monte Carlo all-or-nothing approach for coalescence, which greatly enhances the production of lucky drops compared to LSdSDM, is a critical factor governing overall rain initiation in LES using SDM. This is consistent with Telford (1955), who examined stochastic versus continuous coalescence in a simple model, and Wilkinson (2016) based on statistical analysis using large deviation theory. It is demonstrated here using a detailed 3D cloud model with Lagrangian particle-based microphysics.

Finally, it is worth pointing out that highly lucky drops (those experiencing several times higher than the expected number of coalescence events) will be severely under-sampled in typical LES configurations using SDM. This is demonstrated by modeling the number of coalescence events a drop experiences as a Poisson distribution[4]. For the sake of illustration we define lucky drops as having 10 times the expected value in number of coalescence events over some time increment, and choose the time interval such that the expected value is 1 coalescence event per drop. It follows that the probability of an individual drop being lucky is $P_r = e^{-1}/10! \approx 10^{-7}$. We can also determine the probability that a finite volume with number N_{tot} of real drops or SDs will contain a lucky drop. Each real drop or SD is treated as an independent trial with $P_r = 10^{-7}$ to estimate whether a lucky drop occurs in the volume, and given the small P_r we can apply the Poisson approximation. For $N_{tot} = 100$, the probability of at least 1 lucky drop in the volume is $\approx 10^{-5}$. For $N_{tot} = 10^6$, the probability is ≈ 0.095 (slightly less than $P_r N_{tot} = 0.1$ because rarely some volumes

[4]This calculation assumes a constant rate parameter for simplicity but the expected number of coalescence events will increase over time for drops because the collection kernel for a drop increases as it grows by coalescence.

will have 2 or more lucky drops). In a typical LES grid cell volume of $O\left(10^3\right)$ m^3 with at least 10^{10} real drops, the probability of having at least one lucky drop in the volume is nearly 1 with an expected number of lucky drops $\sim 10^3$. Because SD multiplicity is generally $\gg 1$, when lucky SDs do occur with SDM they are associated with a large number of individual drops. However, for typical LES configurations ($\sim 10^2$ SDs within a grid cell), lucky drops are unlikely to be sampled in the vast majority of grid cells. This paints the picture of SDM having excessive variance in the number of coalescence events compared to a population of real drops (Shima et al. 2009), but under-representing the frequency that lucky drops occur throughout a cloud, especially at low N_{SD}.

Given the huge number of drops in real clouds (easily 10^{17} in a 1 km^3 cloud), it is clear that even extremely lucky drops (say, one in 10^{12}) will be practically ubiquitous in any cloud that has an active coalescence process. One could take this to imply that the Smoluchowski approach should be better than discrete particle-based methods given that the practical limit on N_{SD} is vastly smaller than the number of real drops in a cloud. However, the Smoluchowski equation is fundamentally incompatible with Lagrangian particle-based microphysics without additional steps such as mapping/re-mapping between the discrete and continuum DSDs as in Andrejczuk et al. (2010). Moreover, based on our LES results, including some evidence for convergence of integrated rain properties for $N_{SD} \geq 256$, better representing lucky drops by increasing N_{SD} beyond that tested here would likely further increase rain fraction but with a compensating decrease of the "in rain" water content, thus leading to little change in bulk rain properties. Testing this hypothesis will require additional runs in the future with larger N_{SD}, imposing a significant computational cost.

Acknowledgments. HM, KKC, and WWG were supported by the U.S. Department of Energy (DOE) Atmospheric System Research grant DE-SC0020118. Additional support for HM and KKC was provided by DOE Office of Biological and Environmental Research (BER) Earth System Model Development (ESMD) grant DE-SC0023151. This material is based upon work supported by the NSF National Center for Atmospheric Research, which is a major facility sponsored by the National Science Foundation under Cooperative Agreement No. 1852977. We acknowledge high-performance computing support from Cheyenne (doi:10.5065/D6RX99HX) provided by NSF NCAR's Computational and Information Systems Laboratory. We thank Dr. George Bryan for developing and maintaining CM1. SS was supported by JSPS KAKENHI, Grant Number 20H00225 and 23H00149; and JST [Moonshot R & D][Grant Number JPMJMS2286]. PD was supported by the Polish National Science Center grant no 2018/31/D/ST10/01577 and by the European Union's Horizon 2020 research and innovation programme under Grant Agreement 101003470, project Next Generation Earth Modelling Systems (NextGEMS). We thank Dr. Zachary Lebo and two anonymous reviewers whose comments improved the paper.

Data availability statement. The current study used the CM1 model (`https://www2.mmm.ucar.edu/people/bryan/cm1/`) release 19.8 for the simulations presented here. The SDM and Lagrangian microphysics code is available at `https://github.com/Shima-Lab/SCALE-SDM_BOMEX_Sato2018`. The model outputs used in this study are too large to archive. Instead, the input and namelist files for the simulation runs and the box microphysics model will be made available upon request to the first author.

APPENDIX

Here we further explore variability in rain evolution in the box simulations and sensitivity to the model step. We analyze the rain mass fraction F_r, defined as the mass contained in rain-sized drops ($r \geq 40$ μm) divided by total liquid mass. Figure A1 shows timeseries of F_r from each member (realization) using SDM, LSdSDM, and LSAIM and $N_{SD} = 128$. Results for fSDM are similar to SDM, with similar spread and slightly reduced mean F_r (not shown). The ensemble mean time to reach a given value of F_r, $\overline{t(F_r)}$, is illustrated by red lines in Fig. A1a-c. Values of $\overline{t(F_r)}$ correspond to the ensemble mean rain initiation time considering threshold values of F_r from 0.01 to 0.9. The $\overline{t_{10}}$ values in Fig. 3 correspond to $\overline{t(F_r = 0.1)}$. $\overline{t(F_r)}$ is about 200-300 sec

faster for LSAIM than SDM across the range of F_r (Fig. A1d). LSdSDM is also faster than SDM to reach small F_r (< 0.2), but for $F_r > 0.2$ it is close to SDM. Consistent with our earlier analysis of $\sigma_{t10}/\overline{t_{10}}$, ensemble variability is much greater for SDM than LSAIM and LSdSDM as seen by the spread of individual ensemble members in Fig. A1a-c.

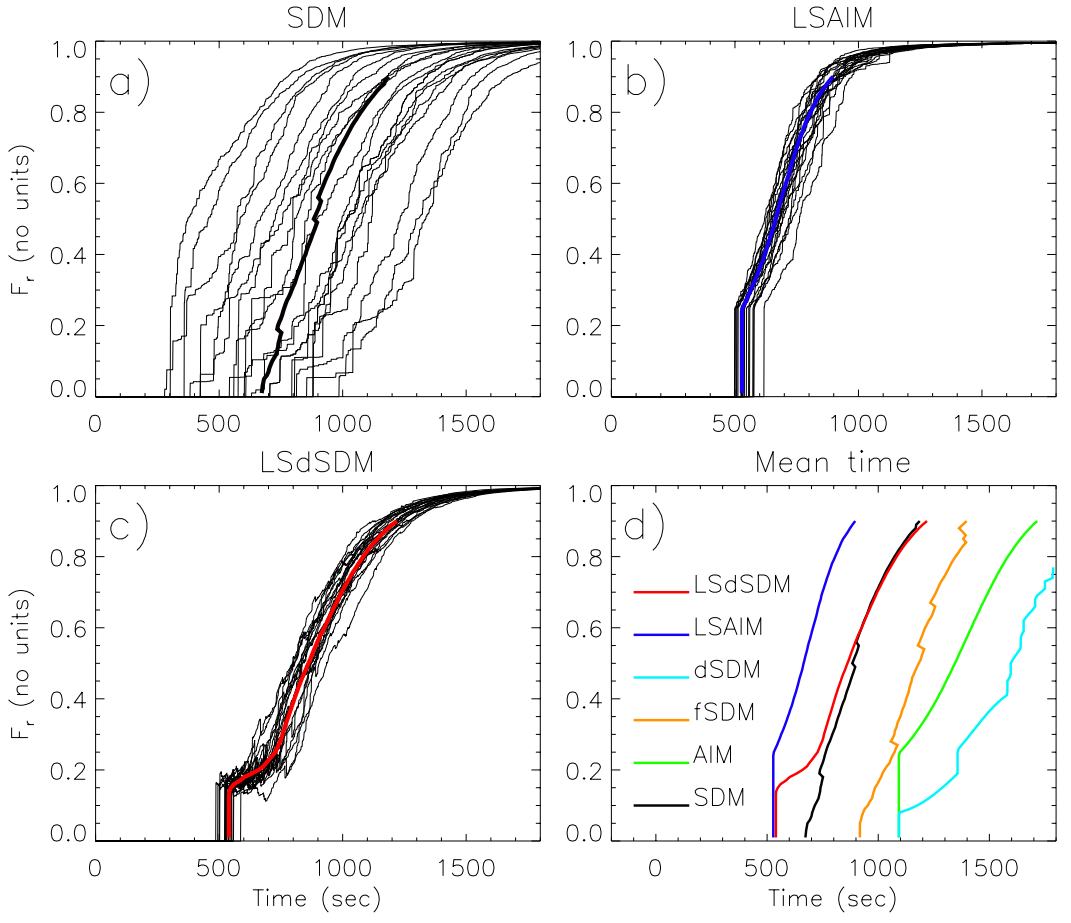

FIG. A1. Timeseries of the fraction of condensate occurring as rain sized drops (radius ≥ 40 μm), F_r, from the box model for a) SDM, b) LSAIM, and c) LSdSDM. Results are shown for N_{SD} = 128. Individual ensemble members are indicated by black lines, and red lines show the mean time for ensemble members to reach a given value of F_r. The mean times for SDM, LSAIM, and LSdSDM to reach a given F_r are compared in d).

Figure A2 shows curves of F_r as a function of time for each ensemble member using SDM and N_{SD} from 32 to 8192. Also shown are curves of $\overline{t(F_r)}$ versus F_r (red lines) and t versus the ensemble mean F_r at a given time, $\overline{F_r(t)}$ (green lines). The latter gives the rain initiation time for the ensemble as a whole, in which a single member with rain drops will lead to $\overline{F_r(t)} > 0$. Consistent with $\sigma_{t10}/\overline{t_{10}}$ in Fig. 4, the decrease of ensemble variability with increasing N_{SD} is

clear. At $N_{SD} = 32$, a few members that produce rain drops quickly, associated with large ensemble variability, lead to rapid rain production for the ensemble as a whole, with $\overline{F_r(t)} > 0.01$ for t greater than about 300 sec (green line). This occurs despite slow rain initiation for the ensemble mean with $\overline{t(F_r > 0.01)}$ greater than ≈ 1000 sec (red line). As N_{SD} is increased, there is little change in $\overline{F_r(t)}$ at small values of F_r, meaning the timing of rain production for the ensemble as a whole is insensitive to N_{SD}. That is, overall rain production for an ensemble is determined by its members that are the fastest to produce rain, and the timing of rain production in these members is insensitive to N_{SD}. This has implications for the timing of rain in the LES (see section 4), since the LES cloud can be understood as an ensemble of separate collision volumes corresponding to the model spatial grid. On the other hand, the ensemble mean time for rain initiation decreases with N_{SD}, indicated by the decrease in $\overline{t(F_r)}$ at small values of F_r. This is consistent with the decrease in $\overline{t_{10}}$ with increasing N_{SD} seen in Fig. 3. For $N_{SD} \geq 512$, curves of $\overline{F_r(t)}$ and $\overline{t(F_r)}$ approach one another and are nearly equal at $N_{SD} = 8192$. This occurs because as N_{SD} is increased, every ensemble member can better represent coalescence fluctuations and lucky drops, whereas such fluctuations lead to variability among ensemble members at low N_{SD}.

The sensitivity of t_{10} to Δt also highlights differences among the coalescence methods. Differences in $\overline{t_{10}}$ and $\sigma_{t10}/\overline{t_{10}}$ using Δt of 0.1, 1, or 10 sec for SDM, LSdSDM, and LSAIM are shown in Fig. A3. Differences are calculated relative to values using $\Delta t = 1$ sec and shown across the range of N_{SD}. Differences are generally much smaller between Δt of 0.1 and 1 sec than between 1 and 10 sec. For instance, relative differences in $\overline{t_{10}}$ between $\Delta t = 0.1$ and 1 sec for SDM are within 15% over the range of N_{SD}, and 3% when averaged over this range. Relative differences increase to a maximum of 18% and mean of 13% between $\Delta t = 1$ and 10 sec over the range of N_{SD}. Similar results for SDM are seen for $\sigma_{t10}/\overline{t_{10}}$ (Fig. A3b). Based on these results, it appears that coalescence is reasonably converged using SDM at $\Delta t = 1$ sec. This supports previous findings of Unterstrasser et al. (2017, 2020).

Overall, there is greater sensitivity to Δt for LSdSDM and LSAIM compared to SDM, particularly for ensemble variability as quantified by $\sigma_{t10}/\overline{t_{10}}$. Ensemble variability using LSdSDM and LSAIM is driven solely by stochastic linear sampling of SD coalescence pairs. Relative to the coalescence timescale, larger Δt implies less frequent sampling of SD pairs which may possibly coalesce, thus increasing variability. As $\Delta t \to 0$, the stochastic linear sampling approaches full sampling and

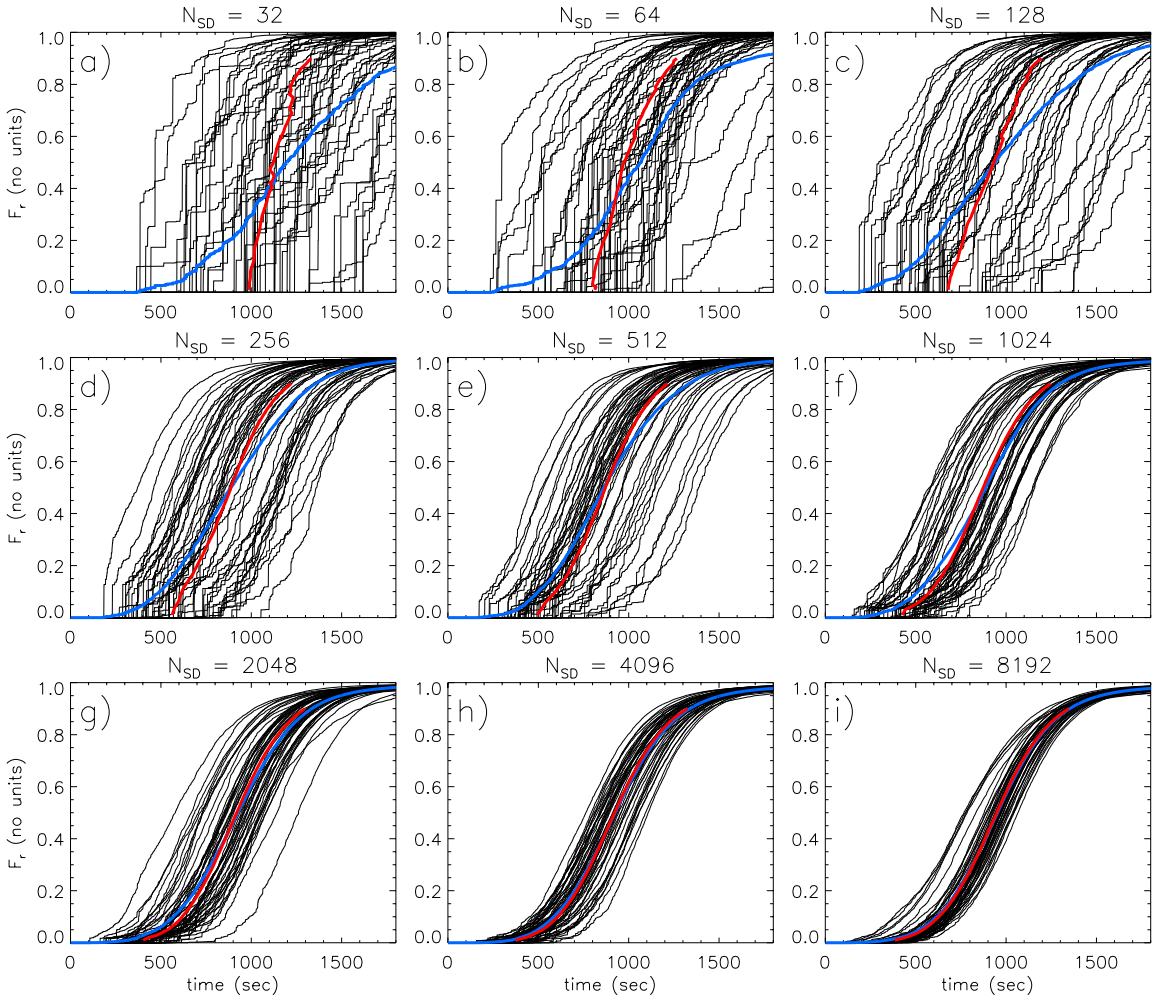

FIG. A2. Timeseries of the fraction of condensate occurring as rain sized drops (radius $\geq 40\ \mu$m), F_r, from the box model using SDM for various N_{SD} from 32 to 8192 as labeled. Individual ensemble members are indicated by black lines, red lines show the mean time for ensemble members to reach a given value of F_r, $\overline{t(F_r)}$, and green lines show show ensemble mean F_r at a given time, $\overline{F_r(t)}$.

thus variability in LSdSDM and LSAIM would be expected to approach 0. Indeed, they give a substantial reduction in $\sigma_{t10}/\overline{t_{10}}$ between $\Delta t = 10$ and 1 sec and between 1 and 0.1 sec (Fig. A3b). In contrast, there is little sensitivity of $\sigma_{t10}/\overline{t_{10}}$ to Δt for SDM because variability in SDM is dominated by the Monte Carlo all-or-nothing coalescence scheme rather than the linear sampling of SD pairs.

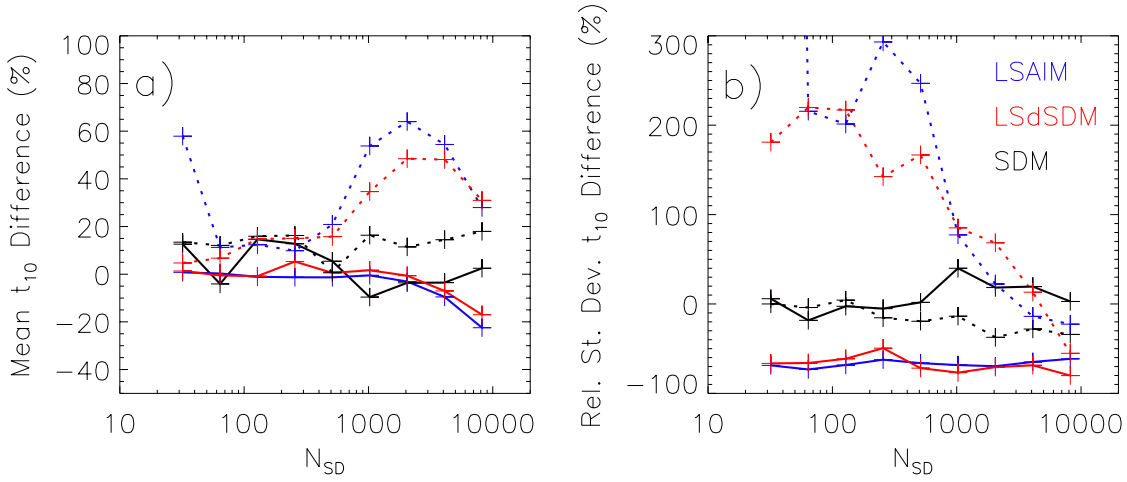

FIG. A3. Relative difference in a) ensemble mean $\overline{t_{10}}$ and b) relative standard deviation $\sigma_{t10}/\overline{t_{10}}$ from the box model simulations between $\Delta = 0.1$ and 1 sec (solid lines) and between 1 and 10 sec (dotted lines) over the range of N_{SD}. Results are shown for LSAIM (blue), LSdSDM (red), and SDM (black). Percentage differences are calculated relative to results using $\Delta t = 1$ sec.

References

Andrejczuk, M., W. W. Grabowski, J. M. Reisner, and A. Gadian, 2010: Cloud-aerosol interactions for boundary layer stratocumulus in the Lagrangian Cloud Model. *J. Geophys. Res.*, **115**, D22 214, doi:10.1029/2010JD014 248.

Arabas, S., A. Jaruga, H. Pawlowska, and W. W. Grabowski, 2015: Libcloudph++ 1.0: a single-moment bulk, double-moment bulk, and particle-based warm-rain microphysics library in C++. *Geosci. Model Dev.*, **8**, 1677–1707.

Arabas, S., and S.-I. Shima, 2013: Large-eddy simulations of trade wind cumuli using particle-based microphysics with Monte Carlo coalescence. *J. Atmos. Sci.*, **70 (9)**, 2768–2777.

Bayewitz, M. H., J. Yerushalmi, S. Katz, and R. Shinnar, 1974: The extent of correlations in a stochastic coalescence process. *J. Atmos. Sci.*, **31**, 1604–1614.

Brdar, S., and A. Seifert, 2018: McSnow: A Monte-Carlo particle model for riming and aggregation of ice particles in a multidimensional microphysical phase space. *J. Adv. Model. Earth Sys.*, **10**, 187–206.

Bryan, G. H., and J. M. Fritsch, 2002: A benchmark simulation for moist nonhydrostatic numerical models. *Monthly Weather Review*, **130 (12)**, 2917–2928.

Chandrakar, K. K., W. W. Grabowski, H. Morrison, and G. H. Bryan, 2021: Impact of entrainment-mixing and turbulent fluctuations on droplet size distributions in a cumulus cloud: An investigation using lagrangian microphysics with a sub-grid-scale model. *Journal of the Atmospheric Sciences*, **78**, 2983–3005.

Chandrakar, K. K., H. Morrison, W. W. Grabowski, and G. H. Bryan, 2022: Comparison of lagrangian "super-droplet" and eulerian double-moment spectral microphysics schemes in large-eddy simulations of an isolated cumulus-congestus cloud. *Journal of the Atmospheric Sciences*, **79**, 1887–1910.

Deardorff, J. W., 1980: Stratocumulus-capped mixed layers derived from a three-dimensional model. *Bound. Lay. Meteor.*, **18**, 495–527.

Dziekan, P., J. B. Jensen, W. W. Grabowski, and H. Pawlowska, 2021: Impact of giant sea salt aerosol particles on precipitation in marine cumuli and stratocumuli: Lagrangian cloud model simulations. *J. Atmos. Sci.*, **78**, 4127–4142.

Dziekan, P., and H. Pawlowska, 2017: Stochastic coalescence in lagrangian cloud microphysics. *Atmospheric Chemistry and Physics*, **17 (22)**, 13 509–13 520.

Dziekan, P., M. Waruszewski, and H. Pawlowska, 2019: University of Warsaw Lagrangian Cloud Model (UWLCM) 1.0: a modern large-eddy simulation tool for warm cloud modeling with Lagrangian microphysics. *Geosci. Model Dev.*, **12**, 2587–2606.

Feingold, G., S. Tzivion, and Z. Leviv, 1988: Evolution of raindrop spectra. Part I: Solution to the stochastic collection/breakup equation using the method of moments. *Journal of Atmospheric Sciences*, **45 (22)**, 3387–3399.

Golovin, A. M., 1963: The solution of the coagulation equation for cloud droplets in a rising air current. *Bull. Acad. Sci. USSR, Geophys. Ser.*, **5**, 783–791.

Grabowski, W. W., 2014: Extracting microphysical impacts in large-eddy simulations of shallow convection. *J. Atmos. Sci.*, **71**, 4493–4499.

Grabowski, W. W., P. Dziekan, and H. Pawlowska, 2018: Lagrangian condensation microphysics with Twomey CCN activation. *Geoscientific Model Development*, **11 (1)**, https://doi.org/10.5194/gmd-11-103-2018.

Grabowski, W. W., and D. Jarecka, 2015: Modeling condensation in shallow nonprecipitating convection. *J. Atmos. Sci.*, **73**, 4661–4679.

Grabowski, W. W., and H. Morrison, 2016: Untangling microphysical impacts on deep convection applying a novel modeling methodology. Part 2: Double-moment microphysics. *J. Atmos. Sci.*, **73**, 3749–3770.

Grabowski, W. W., H. Morrison, S.-I. Shima, G. C. Abade, P. Dziekan, and H. Pawlowska, 2019: Modeling of cloud microphysics: Can we do better? *Bulletin of the American Meteorological Society*, **100 (4)**, 655–672, https://doi.org/10.1175/BAMS-D-18-0005.1.

Hall, W. D., 1980: A detailed microphysical model within a two-dimensional dynamic framework: Model description and preliminary results. *Journal of Atmospheric Sciences*, **37 (11)**, 2486–2507.

Hill, A. A., and Coauthors, 2023: Toward a numerical benchmark for warm rain processes. *J. Atmos. Sci.*, **80**, 1329–1359.

Hoffmann, F., Y. Noh, and S. Raasch, 2017: The route to raindrop formation in a shallow cumulus cloud simulated by a lagrangian cloud model. *Journal of the Atmospheric Sciences*, **74 (7)**, 2125–2142.

Hoffmann, F., S. Raasch, and Y. Noh, 2015: Entrainment of aerosols and their activation in a shallow cumulus cloud studied with a coupled lcm–les approach. *Atmospheric Research*, **156**, 43–57.

Hoffmann, F., T. Yamaguchi, and G. Feingold, 2019: Inhomogeneous mixing in lagrangian cloud models: Effects on the production of precipitation embryos. *Journal of the Atmospheric Sciences*, **76 (1)**, 113–133.

Jaruga, A., and H. Pawlowska, 2018: Libcloudph++ 2.0: Aqueous-phase chemistry extension of the particle-based cloud microphysics scheme. *Geosci. Model Dev.*, **11**, 3623–3645.

Kostinski, A. B., and R. A. Shaw, 2005: Fluctuations and luck in droplet growth by coalescence. *Bulletin of the American Meteorological Society*, **86 (2)**, 235–244.

Lasher-Trapp, S. G., W. A. Cooper, and A. M. Blyth, 2005: Broadening of droplet size distributions from entrainment and mixing in a cumulus cloud. *Quarterly Journal of the Royal Meteorological Society: A journal of the atmospheric sciences, applied meteorology and physical oceanography*, **131 (605)**, 195–220.

Li, X.-Y., B. Mehlig, G. Svensson, A. Brandenburg, and N. E. Haugen, 2022: Collision fluctuations of lucky droplets with superdroplets. *Journal of the Atmospheric Sciences*, **79**, 1821–1835.

Long, A. B., 1974: Solutions to the droplet collection equation for polynomial kernels,. *J. Atmos. Sci.*, **31**, 1040–1052.

Maronga, B., and Coauthors, 2015: The Parallelized Large-Eddy Simulation Model (PALM) version 4.0 for atmospheric and oceanic flows: model formulation, recent developments, and future perspectives. *Geosci. Model Dev.*, **8**, 2515–2551.

Matsumoto, M., and T. Nishimura, 1998: Mersenne Twister: a 623- dimensionally equidistributed uniform pseudo-random number generator. *ACM Transactions on Modeling and Computer Simulation*, **8**, 3–30.

Morrison, H., J. M. Peters, K. K. Chandrakar, and S. C. Sherwood, 2022: Influences of environmental relative humidity and horizontal scale of sub-cloud ascent on deep convective initiation. *Journal of the Atmospheric Sciences*, **79**, 337–359.

Naumann, A. K., and A. Seifert, 2015: A Lagrangian drop model to study warm rain microphysical processes in shallow cumulus. *Journal of Advances in Modeling Earth Systems*, **7 (3)**, 1136–1154.

Noh, Y., D. Oh, F. Hoffmann, and S. Raasch, 2018: A cloud microphysics parameterization for shallow cumulus clouds based on Lagrangian cloud model simulations. *J. Atmos. Sci.*, **75**, 4031–4047.

Riechelmann, T., Y. Noh, and S. Raasch, 2012: A new method for large-eddy simulations of clouds with lagrangian droplets including the effects of turbulent collision. *New Journal of Physics*, **14 (6)**, 065 008.

Schwenkel, J., F. Hoffmann, and S. Raasch, 2018: Improving collisional growth in Lagrangian cloud models: development and verification of a new splitting algorithm. *Geosci. Model Dev.*, **11**, 3929–3944.

Shima, S.-I., K. Kusano, A. Kawano, T. Sugiyama, and S. Kawahara, 2009: The super-droplet method for the numerical simulation of clouds and precipitation: A particle-based and probabilistic microphysics model coupled with a non-hydrostatic model. *Quarterly Journal of the Royal Meteorological Society*, **135 (642)**, 1307–1320.

Shima, S.-I., Y. Sato, A. Hashimoto, and R. Misumi, 2020: Predicting the morphology of ice particles in deep convection using the super-droplet method: development and evaluation of scale-sdm 0.2. 5-2.2. 0,-2.2. 1, and-2.2. 2. *Geoscientific Model Development*, **13 (9)**, 4107–4157.

Sölch, I., and B. Kärcher, 2010: A large-eddy model for cirrus clouds with explicit aerosol and ice microphysics and Lagrangian ice particle tracking. *Quart. J. Roy. Meteor. Soc.*, **136**, 2074–2093.

Stevens, B., G. Feingold, W. R. Cotton, and R. L. Walko, 1996: Elements of the microphysical structure of numerically simulated nonprecipitating stratocumulus. *Journal of Atmospheric Sciences*, **53 (7)**, 980–1006.

Telford, J. W., 1955: A new aspect of coalescence theory. *J. Meteor.*, **12**, 436–444.

Twomey, S., 1966: Computations of rain formation by coalescence. *J. Atmos. Sci.*, **23**, 405–411.

Tzivion, S., G. Feingold, and Z. Levin, 1987: An efficient numerical solution to the stochastic collection equation. *Journal of Atmospheric Sciences*, **44 (21)**, 3139–3149.

Tzivion, S., G. Feingold, and Z. Levin, 1989: The evolution of raindrop spectra. Part II: Collisional collection/breakup and evaporation in a rainshaft. *Journal of the Atmospheric Sciences*, **46 (21)**, 3312–3328.

Unterstrasser, S., F. Hoffmann, and M. Lerch, 2017: Collection/aggregation algorithms in Lagrangian cloud microphysical models: Rigorous evaluation in box model simulations. *Geosci. Model Dev.*, **10**, 1521–1548.

Unterstrasser, S., F. Hoffmann, and M. Lerch, 2020: Collisional growth in a particle-based cloud microphysical model: insights from column model simulations using lcm1d (v1. 0). *Geoscientific Model Development*, **13 (11)**, 5119–5145.

Unterstrasser, S., and I. Sölch, 2014: Optimisation of the simulation particle number in a lagrangian ice microphysical model. *Geosci. Model Dev.*, **7**, 695–709.

VanZanten, M. C., and Coauthors, 2011: Controls on precipitation and cloudiness in simulations of trade-wind cumulus as observed during RICO. *Journal of Advances in Modeling Earth Systems*, **3 (2)**, MS000 056, doi/10.1029/2011MS000 056.

Weil, J. C., P. P. Sullivan, and C.-H. Moeng, 2004: The use of large-eddy simulations in Lagrangian particle dispersion models. *Journal of the Atmospheric Sciences*, **61 (23)**, 2877–2887.

Wilkinson, M., 2016: Large deviation analysis of rapid onset of rain showers. *Phys. Rev. Lett.*, **116**, 018 501, doi:10.1103/PhysRevLett.116.018 501.

Zmijewski, P., P. Dziekan, and H. Pawlowska, 2023: Modeling collision-coalescence in particle microphysics: Numerical convergence of mean and variance of precipitation in cloud simulations using University of Warsaw Lagrangian Cloud Model (UWLCM) 2.1. *Geosci. Model Dev. Discuss.*, **(in review)**, doi:10.5194/gmd–2023–44.